American Society of Mechanical Engineers

ASME Accepted Manuscript Repository

Institutional Repository Cover Sheet

Cranfield Collection of E-Research - CERES

ASME Paper Title: Insights into the flow field and performance of a boundary layer pump

Authors: David John Rajendran, Kyril Palaveev, Eduardo Anselmi, Mani Santhanakrishnan, Vassilios Pachidis

ASME Journal Title: Journal of Engineering for Gas Turbines and Power

Volume/Issue: Volume 146, Issue 6 Date of Publication (VOR* Online): 19 October 2023

ASME Digital Collection URL: https://asmedigitalcollection.asme.org/gasturbinespower/article/doi/10.1115/1.4063834/1169585/Insights-Into-the-Flow-Field-and-Performance-of-a

DOI: https://doi.org/10.1115/1.4063834

*VOR (version of record)

Journal of Engineering for Gas Turbines and Power, Volume 146, Issue 6, June 2024,
Article number 061002, Paper number GTP-23-1390
DOI:10.1115/1.4063834

INSIGHTS INTO THE FLOW FIELD AND PERFORMANCE OF A BOUNDARY LAYER PUMP

Kyril Palaveev, David John Rajendran*, Eduardo Anselmi, Mani Santhanakrishnan, Vassilios Pachidis

Cranfield University, Cranfield, UK

ABSTRACT

A flow field analysis of a realistic, integrated, multi-disc boundary layer pump as is necessary for investigating the reasons for typically quoted low efficiencies in such pumps is described. The study focuses on the 3D RANS solutions of a water boundary layer pump model created to replicate a design by Morris, 1973, which consists of 170 discs and a volute channel. A baseline study is performed to investigate the rotor-only performance after which a volute alone is separately simulated to identify the performance and losses in each as separate systems. Thereafter, an integrated model is characterized across mass flow rates and rotational speeds. The flow fields of all three models are discussed and the results of the integrated model are compared to the experimental data.

The results from the model with the rotor only confirm the typically made claim that the efficiency of the rotor in a boundary layer pump possesses relatively high values which in this case is 87% at the design point, reinforcing results from previous studies that the rotor assembly is not the cause of inefficiency. The volute on its own indicated a hydraulic efficiency of around 97%. However, the integrated model yielded a rotor efficiency of around 74% and an overall pump efficiency of 51% at the design point, clearly outlining the fact that the effect of the volute integrated with the rotor is the reason for both the rotor and pump efficiency degradataion. The reason for this drop in efficiency is discussed in detail by highlighting the change in the flow topologies. The insights into the flow field and the identification of the reason for inefficiencies using a separated component analysis approach provides directions for avenues in which design improvements would need to be attempted.

Keywords: Boundary Layer Pump, Tesla Pump, Friction Pump, Computational Fluid Dynamics

NOMENCLATURE

u	Velocity in x $[m/s]$
v	Velocity in y $[m/s]$
w	Velocity in z $[m/s]$
T	Temperature $[K]$
p	Static pressure $[Pa]$
p_0	Total pressure $[Pa]$
λ	Molecular thermal conductivity $[W/mK]$
λ_t	Turbulent thermal conductivity $[W/mK]$
μ	Dynamic viscosity $[Pas]$
ε	Turbulence dissipation rate $[W/kg]$
$\lvert\hat{S}\rvert$	Strain rate tensor $[1/s]$
$\dot{S}_D$	Direct entropy generation rate $[W/m^3K]$
$\dot{S}_I$	Indirect entropy generation rate $[W/m^3K]$
$\dot{S}_{\partial\bar{T}}$	Mean gradient heat conduction entropy generation rate $[W/m^3K]$
$\dot{S}_{\partial T'}$	Fluctuating gradient heat conduction entropy generation rate $[W/m^3K]$
$\dot{S}$	Total entropy generation rate $[W/kg]$
Q	Volumetric flow rate $[m^3/s]$
J	Torque $[Nm]$
ω	Rotational speed $[rad/s]$
η_{hyd}	Hydraulic efficiency $[-]$

1. INTRODUCTION

Boundary layer pumps have become an increasingly researched area of alternative turbomachinery due to their simplistic design of concentrically stacked, smooth discs, offering a more cost-effective solution to conventional, bladed turbomachinery [1–17]. A boundary layer pump's working principle is based on the Coanda effect [18] and kinetic energy is transmitted from the rotor to the fluid only by frictional forces which makes boundary layer pumps more suitable for some specific applications such as non-Newtonian fluids at which bladed turbomachinery cannot operate efficiently. However, boundary layer turbomachinery that have been constructed in research works are reported in the literature to have low experimental overall efficiencies (Figure 1) compared to centrifugal machines, even though theoretical modelling suggests high efficiencies, comparable to those of centrifugal machines [2, 5, 10, 14]. Moreover, works on boundary layer pumps have not been reported as much as boundary layer turbines. Significantly, only two recent studies have noted and attempted to describe the large discrepancies between design expectations and experiments. Medvitz et al.[8] performed 3D RANS solutions on a high fidelity boundary layer left ventricular assist device (LVAD) model comprising of 11 discs, an axial inlet, and a double channel volute. Medvitz et al. [8] performed

*Corresponding author: d.rajendran@cranfield.ac.uk

Published by The American Society of Mechanical Engineers. This is the Author Accepted Manuscript issued with:
Creative Commons Attribution License (CC BY). The final published version is available online at DOI:10.1115/1.4063834.
Please refer to any applicable publisher terms of use.

multiple design iterations and achieved a pump with a theoretical overall efficiency of approximately 18%, which is significantly lower than what a 1D analytical solution would yield [2, 11, 14]. Despite producing multiple changes to the inlet arrangement of the discs and the volute, Medvitz et al. [8] did not investigate the root cause of the performance losses by examining key components of the pump separately. Following that, Wang et al. [7] developed a high fidelity 3D RANS model of a water pump with 7 discs and also performed experimental validation. One of the main outcomes from the study performed by Wang et al. [7] is the good agreement between experimental and numerical results, reinforcing that high fidelity 3D RANS models of boundary layer pumps comprising of axial inlets, multiple discs, and volute outlets are a suitable approach to more accurately estimating the efficiency of such pumps theoretically. Wang et al. [7] also set out to investigate the performance of the discs and volute channel separately through 3D RANS solutions to conclude that the rotor performance alone is in fact comparable to that of a bladed centrifugal machine and that an integrated pump with a volute causes significant performance losses peaking at 40% overall efficiency. Wang et al. [7], however, did not present a detailed flow field analysis of the 3D RANS solutions which is necessary in order to understand the source of major losses. Furthermore, Wang et al. [7] employed a laminar treatment for the rotor-only simulations under the assumption that the flow within the rotor is laminar only and after it was satisfactorily compared with the Spalart-Allmaras (S-A) turbulence model. The S-A turbulence model was also used by Wang et al. [7] to model the volute flow, despite that the S-A model is not recommended for use in models where free shear flows are likely [19], such as the flows leaving the rotor assembly into the volute channel.

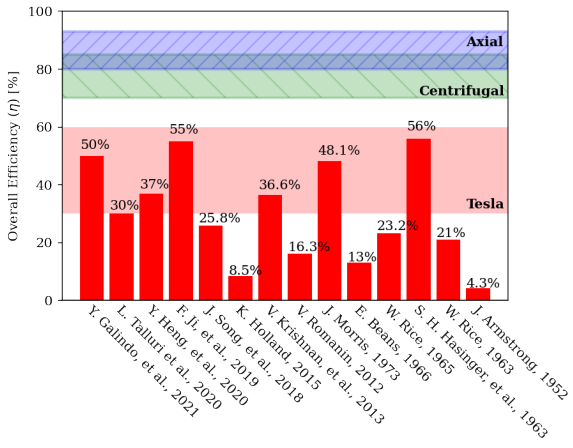


FIGURE 1: A COLLECTION OF BOUNDARY LAYER / TESLA TURBOMACHINERY (PUMPS AND TURBINES) EFFICIENCIES OBTAINED EXPERIMENTALLY.[1–6, 10–17]. FOR COMPARISON, TYPICAL CENTRIFUGAL [20] AND AXIAL [21] TURBOMACHINERY EFFICIENCIES ARE ALSO PLOTTED.

In order to define concrete solutions for tackling the low efficiencies of boundary layer pumps, it is necessary to understand the reason for the losses through a detailed flow field analysis of a boundary layer pump. Because such a study with a focus to delineate the loss mechanisms has not been performed as of yet, the root cause of the efficiency loss remains to be described and identified. Such a study would provide guidelines for the development of appropriate methods for improving the efficiency. With this objective, a detailed flow field analysis of a boundary layer pump is performed from flow field solutions obtained through a set of directed 3D RANS solutions. The investigation begins with a benchmark assessment of a rotor-only, multi-disc model, followed by the examination of a volute-only model to assess the performance of the volute, and finally concluding with a fully integrated pump comprised of 170 discs and a volute channel outlet. From separate and combined considerations of the three sets of the solutions, the flow fields are assessed to describe dominant flow mechanisms and the interaction between the components. Some modifications to the models are also implemented in order to present a preliminary, potential mitigation strategy for combating the low efficiencies.

2. METHODOLOGY

2.1 Model

The computational model for the present study is obtained from an extensive, parametric, experimental study of boundary layer pumps, performed by Morris [13]. The experimental study by Morris consisted of multiple pumps with different rotor diameters, number of discs, inter-disc spacings, and number of diffusers in the diffuser rings prior to the scroll volute channel. All of the pumps typically conformed to the basic setup of a boundary layer pump comprised of an axial inlet, a rotor of multiple discs, and a volute outlet channel. The experimental testing of the different pumps at different rotational speeds and mass flow rates with water as the working fluid is described in Morris' report [13]. Detailed experimental measurements to describe the pump performance that include the pump inlet and outlet static pressures, flow rates using a turbine flow meter, drive shaft rotational speed using a tachometer and torque via a dynamometer, temperature at the inlet, and a pitot-static tube tangentially oriented to the rotor outlet to measure the rotor outlet conditions separately are included in the report. The efficiency of the pump rotor alone is calculated from the rotor inlet conditions and pitot-static tube readings at the outlet. The experimental overall efficiency of the pump, including the intake and volute losses, are calculated based on the pump inlet and outlet conditions. To perform the overall pump efficiency calculations, the actual power input into the pump rotor is measured using a torque meter installed on the drive shaft.

One of the reported by Morris [13] pump designs is used in this study to provide insights into the flow field evolution. The geometric properties and test conditions of the modeled pump in this study are listed in Table 1. The complete volute geometry is recreated using the Stepanoff and Pfleiderer method, because not all feature of the volute were reported by Morris [13]. All the key geometric and design parameters noted in the report about the volute design are matched. The highlighted with an asterisks parameters in Table 1 are specific to Stepanoff's method. The K_{cm} coefficient is a non-dimensional constant derived by Stepanoff [22] from volute outlet channel experiments along with a set of empirical equations used to design volute geometries. The tangential velocity (c_θ) in the context of volute design is

TABLE 1: SPECIFICATIONS OF THE SIMULATED BOUNDARY LAYER PUMP PROVIDED BY MORRIS, 1973 [13] AND ESTIMATED FROM OTHER MATERIALS FOUND IN [22, 23]. * - REFER TO PARAGRAPH BEFORE TABLE FOR EXPLANATION OF PARAMETERS.

Station	Parameter	Value	Unit
Rotor	Outer diameter (OD)	150.8	$[mm]$
	Inner diameter (ID)	25.4	$[mm]$
	Disc thickness	0.127	$[mm]$
	Inter-disc spacing ($2s$)	0.152	$[mm]$
	Number of discs	170	$[-]$
Volute Channel	Base circle diameter	155.8	$[mm]$
	Radius at $\theta = 360°$	89.22	$[mm]$
	Tongue radius	0.5	$[mm]$
	K_{cm}*	0.27	$[-]$
	Tangential velocity (c_θ)*	12.4	$[m/s]$
	Cross section	Rectangular	$[-]$
	Estimated pump thickness	47.303	$[mm]$
Diffuser	Outlet height	22.3	$[mm]$
	Expansion half-angle	8	$[°]$
Operating Conditions	Fluid type	water	$[-]$
	Inlet total temperature	325	$[K]$
	Inlet total pressure	446	$[kPa]$
	Rotational speed	6000, 7000	$[rpm]$
	Mass flow rate	20, 40, 60, 80, 100	$[gpm]$

computed based on the K_{cm} coefficient and is assumed constant throughout the volute channel. This is the fundamental principle behind Stepanoff's volute channel design technique – constant kinetic energy [22].

In this study, that aims to delineate the systematic development of the flow field and its corresponding effect on the pump performance, three separate models are conceived as presented in Figure 2. The first model is a rotor-only model with an axial inlet that has one-tenth the number of discs as the baseline pump. This is found to be sufficient for capturing the losses associated with flow turning from the axial inlet to the radial rotor passages and within the rotor passages. The goal of this model is to provide a benchmark rotor-only flow field and performance for the other two models and to validate the observations regarding rotor-only performance in another experimental study and geometry described Wang et al. [7]. The second model is a model of the volute channel only. This is done to assess the flow field and losses of the volute channel separately, without the influence of the rotor, which is typically considered to be the reason behind the compromised performance of boundary layer pumps. The third model is a fully integrated model comprised of 170 discs and the volute channel. The performance and the flow field differences of these three models are compared to make a case for the identification of the factor that leads to the compromised efficiency and thus, pave a way for concentrating design efforts to improve the efficiency of the boundary layer pumps. Lastly, the volute geometry is modified parametrically in order to suppose the preliminary steps necessary to construct a plan for minimizing the discovered loss mechanisms.

2.2 Computational Solution

Specialized domain discretization approaches using novel blocking strategies that ensure adequate resolution of boundary layer pump rotor specific flow features are implemented in the thin, gapped space between the rotor discs. Rigorous grid convergence index (GCI) computations for local and global parameters of interest are performed through the Richardson extrapolation method [24]. Based on the results from the GCI study, it is concluded that a grid size of approximately 100k elements for each rotor passage with a minimum of 10 nodes in the gap between the discs is necessary to ensure that the discretization error in all parameters of interest – pressure ratio and enthalpy change across the rotor – are not more than 1.3% (Figure 4 and Table 2). Furthermore, to ensure adequate treatment of the boundary layer in the gapped space for the selected turbulence model, the y^+ value is approximately 2.5 at the inlet region of the pump and increase nearly linearly up to 3.7 at the outlet of the rotor. In order to generate the flow field solution, boundary conditions in terms of total pressure and temperature are specified at the inlet, and the mass flow rate is specified at the outlet. Appropriate inlet and outlet face for each of the three models are of this 'total-flux' boundary condition pair to ensure similar operating condition as in the test data and robustness of the implicit solver (Figure 3). The disc walls are defined to be rotating walls with a stationary fluid domain in the gap as opposed to having a rotating fluid domain and counter-rotating disc walls after verification of similar flow field solutions from both approaches to further ensure code stability. This approach reduces computational costs associated with rotating reference frame corrections in the governing equations and the dissipative averaging operations associated with frame change models required in rotating-stationary domain interfaces. The walls are set to a no-slip boundary condition. For

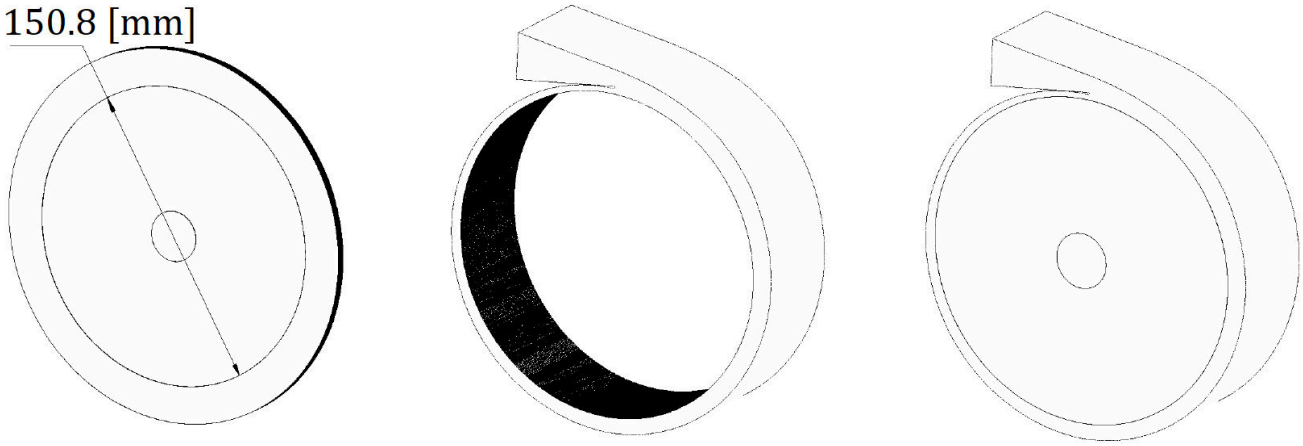


FIGURE 2: DEVELOPED MODELS FOR CURRENT STUDY. (LEFT) – BASELINE MODEL WITH ONE TENTH THE NUMBER OF DISCS FROM THE ORIGINAL GEOMETRY WITH AN ARTIFICIAL OUTLET DOMAIN. (MIDDLE) – VOLUTE ONLY MODEL USED FOR ASSESSING INDIVIDUAL PERFORMANCE OF THE VOLUTE. (RIGHT) – INTEGRATED MODEL WITH 170 DISCS AND VOLUTE OUTLET CHANNEL.

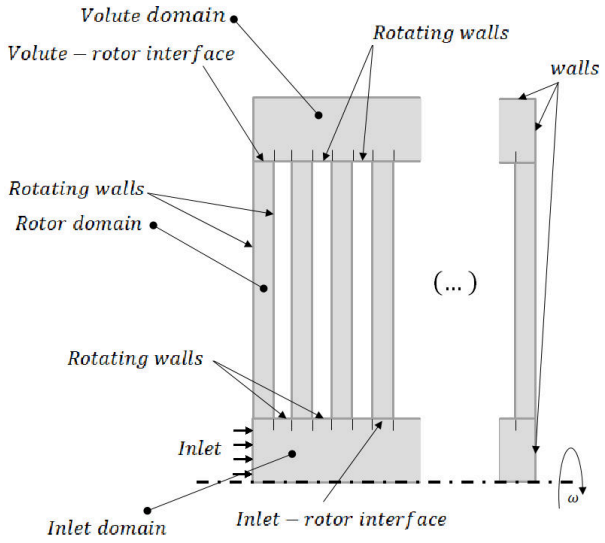


FIGURE 3: DIAGRAM OF MODEL BOUNDARY CONDITIONS. THIS IS A CROSS-SECTIONAL VIEW OF THE ROTOR ASSEMBLY. THE HIGHLIGHTED IN GREY OBJECTS ARE THE FLUID DOMAINS. BLACK LINES INDICATE THE EXISTENCE OF A BOUNDARY CONDITION.

the rotor-only simulation, two artificial domains of cylindrical donut shape are added to the inner and outer diameters of the rotor for numerical reasons in order to constrain the model and specify appropriate boundary conditions. For the volute and integrated simulations, the walls of the volute are stationary, no-slip walls. In the integrated simulations, the rotor and volute are interfaced with a general grid interface boundary condition. The combination of these boundary conditions and interfaces set up a well-defined numerical problem for the solution of the discretized governing equations.

The 3D RANS solutions are carried out in an implicit finite element based finite volume commercial solver, ANSYS CFX 2021.2 [25]. In addition to the boundary conditions, turbulence

TABLE 2: NUMBER OF GRID ELEMENTS FOR EACH MODEL.

Model	Grid element count [-]
Rotor-only	6.5 million
Volute-only	82.0 million
Integrated	241.9 million

closure is specified by using the two-equation k–ω shear stress transport (SST) model because of its known applicability for handling high curvatures and separated flows. Higher resolution second order schemes are used for both advection and turbulence numerics. Explicit wall resolution without resorting to automatic wall functions is ensured. Due to the close node spacings in the inter-disc gap and volute interfaces, an adaptive local timescale factor that computes a zone-specific implicit timestep is considered for the initial pseudo-timestep iterations for pre-conditioning the solution. Thereafter, an advection-based timescale factor is imposed to obtain the converged flow field solution. Convergence of the solutions is declared when maximum threshold residual convergence metrics are below $1e-6$ and parametric convergence metric variations for performance and flux parameters are below 0.1% for at least 100 iterations. All the simulations are performed using a message passing interface based parallelization scheme in a high-performance computing facility 'DELTA' at Cranfield University that has 192 CPUs with a shared memory of 15 TB. Several pre-conditioning related memory control allocations and the topology estimation factors for the interpolator, partitioner, and solver are explicitly specified for appropriately utilizing multiple cores. To reach convergence, the baseline, volute only, and integrated case required approximately 1 hour, 12 hours, and 40 hours of wall-clock time respectively.

2.3 Entropy Generation Rate Computations

The entropy generation rate characterizes the irreversibility in a system and in this study, it is used to quantify and compare losses at different locations [26, 27]. For RANS solutions,

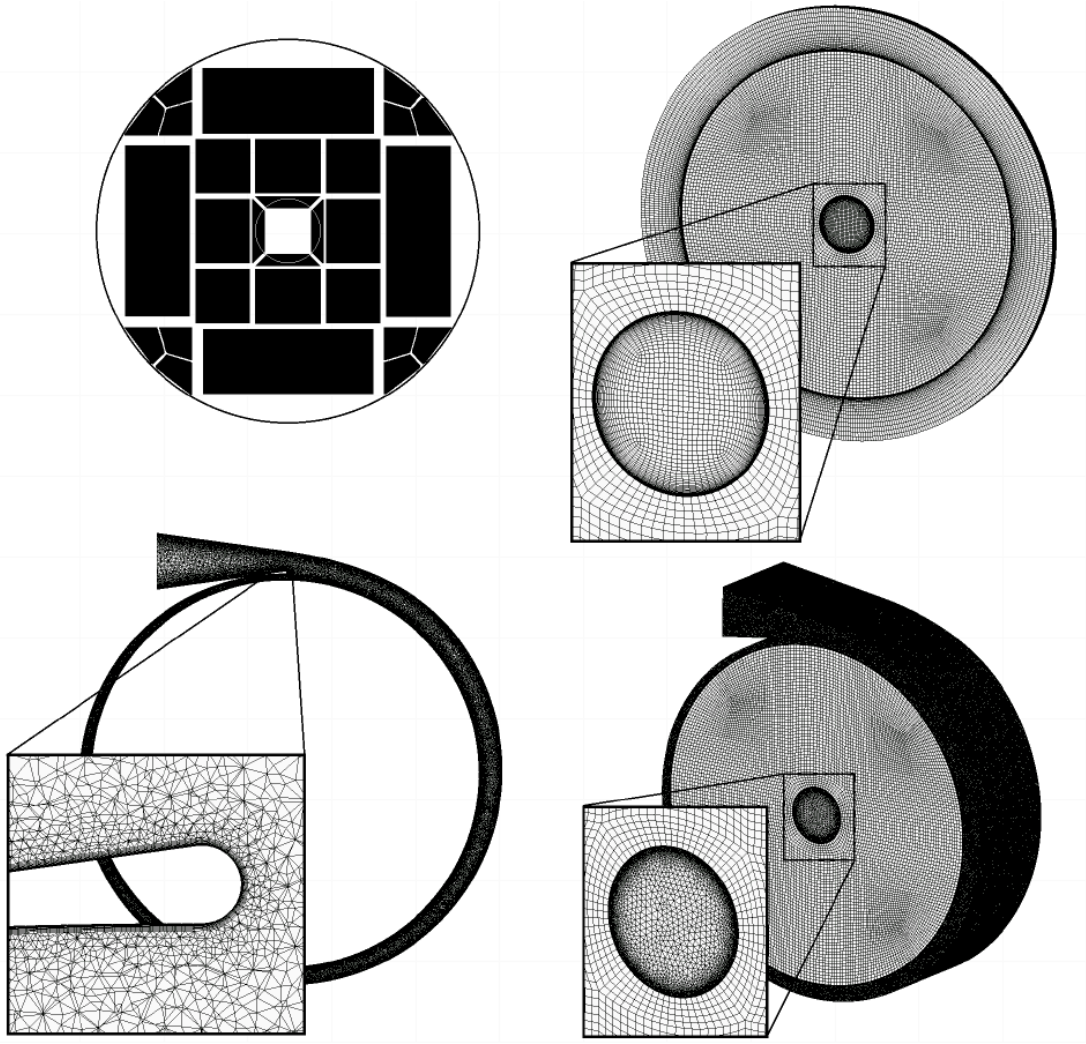


FIGURE 4: DEVELOPED GRIDS FOR THE THREE MODELS. (TOP LEFT) – GRID TOPOLOGY FOR DISC GAPPED SPACE. (TOP RIGHT) – BASELINE MODEL WITH ONE-TENTH THE NUMBER OF DISCS AND ARTIFICIAL OUTLET DOMAIN. (BOTTOM LEFT) – VOLUTE OUTLET CHANNEL GRID. (BOTTOM RIGHT) – INTEGRATED MODEL WITH 170 DISCS AND VOLUTE CHANNEL.

the entropy transport equation must also be in a time-averaged form. Therefore, for each entropy production mechanism, a time-averaged component is used. These components are:

- Direct entropy generation rate ($\dot{S}_D$)
- Indirect entropy generation rate ($\dot{S}_I$)
- Heat conduction entropy generation rate due to mean temperature gradients ($\dot{S}_{\bar{\partial}\bar{T}}$)
- Heat conduction entropy generation rate due to fluctuating temperature gradients ($\dot{S}_{\partial T'}$)

To compute the direct entropy production rate, the strain rate tensor is defined as [26]:

$$|\hat{S}| = \left[2\left(\left(\frac{\partial u}{\partial x}\right)^2 + \left(\frac{\partial v}{\partial y}\right)^2 + \left(\frac{\partial w}{\partial z}\right)^2\right) + \left(\frac{\partial u}{\partial y} + \frac{\partial v}{\partial x}\right)^2 + \left(\frac{\partial u}{\partial z} + \frac{\partial w}{\partial x}\right)^2 + \left(\frac{\partial v}{\partial z} + \frac{\partial w}{\partial y}\right)^2\right]^{1/2} \quad (1)$$

Each entropy production term is then calculated [26]:

$$\dot{S}_D = \frac{\mu}{T}|\hat{S}|^2 \quad (2)$$

$$\dot{S}_I = \frac{\rho\varepsilon}{T} \quad (3)$$

$$\dot{S}_{\bar{\partial}\bar{T}} = \frac{\lambda}{T^2}\left[\left(\frac{\partial T}{\partial x}\right)^2 + \left(\frac{\partial T}{\partial y}\right)^2 + \left(\frac{\partial T}{\partial z}\right)^2\right] \quad (4)$$

$$\dot{S}_{\partial T'} = \frac{\lambda_t}{T^2}\left[\left(\frac{\partial T}{\partial x}\right)^2 + \left(\frac{\partial T}{\partial y}\right)^2 + \left(\frac{\partial T}{\partial z}\right)^2\right] \quad (5)$$

In the above equations, ε refers to the turbulence dissipation rate, λ refers to the molecular thermal conductivity, and λ_t – to the turbulent thermal conductivity. Lastly, the total entropy production rate is defined to be:

$$\dot{S} = \frac{T}{\rho}(\dot{S}_D + \dot{S}_I + \dot{S}_{\partial\bar{T}} + \dot{S}_{\partial T'})[W/kg] \quad (6)$$

Another useful parameter defined below is the Bejan number (Be) [27]. The Bejan number is used to measure the contribution of heat transfer to the total losses. For $Be << 0.5$, the entropy production rate due to fluid friction has a much greater impact on the total energy losses as opposed to the heat conduction entropy production rates and for such Bejan numbers, the heat conduction entropy generation component can be neglected.

$$Be = \frac{\dot{S}_{\partial\bar{T}} + \dot{S}_{\partial T'}}{\dot{S}_{\partial\bar{T}} + \dot{S}_{\partial T'} + \dot{S}_I + \dot{S}_D} \quad (7)$$

3. RESULTS AND DISCUSSION

The results are presented in five sections in which the design point is investigated first, followed by characterizing the performance of the overall pump for different mass flow rates and rotational speeds. The first section presents the findings from the baseline model, which consists of the rotor only. The second section presents the results from the volute-only model which is initialized with the rotor outlet conditions from the rotor-only simulation. The third section is concerned with the results from the integrated model which is the full pump model with 170 discs and the volute outlet channel. The fourth section tackles the flow characterization at different flow rates and rotational speeds for the integrated model. The fifth section presents a potential strategy for increasing the overall pump efficiency of the integrated pump by implementing changes to the volute. The results for all models are presented in the form of cross-sectional contours at different radial and tangential locations of the model. Presenting these contours begins from the inlet towards the outlet of the model. The examined flow properties for each case are the velocity components in cylindrical coordinates, the total and static pressures, and the entropy generation rate as they are considered sufficient for describing the flow field.

3.1 Rotor-only Model

Beginning at the inlet of the pump, a cross-sectional view, along the radius of the rotor at 12 o'clock (known as the 0 degree radial from hereon), is presented in Figure 5. The presented contour spans the thickness of the model and has a radial span of 9.5 [mm] starting from the center line. The flow enters the pump axially on the right-hand side and begins turning radially to enter each of the inter-disc gaps. It is shown by the streamlines that the flow closest to the inlet has a much smaller turning radius than the flow closest to the aft end of the rotor assembly. This is because the flow closer to the inlet has an axial velocity which is higher compared to the axial velocity at the aft discs due to the reduction in total mass flow rate for the same cross-sectional area. Therefore, the axial momentum of the flow cannot be entirely converted into radial momentum at the location it enters the first couple of discs. Nevertheless, due to the relatively low velocity magnitudes, the losses in this region are insignificant which is suggested by the total pressure contour and the entropy generation rate contour with variations across the presented flow field being less than the numerical resolution of the model.

As the flow progresses, in Figure 6, at the interface between the inlet region and the rotor discs, the flow abruptly accelerates radially due to the constriction. It is observed that the radial velocity profile for different disc gaps is different for discs at different axial locations. For the first discs (closer to the inlet), the flow impinges onto the back wall of the disc, causing the velocity profile across the disc spacing to be asymmetric. This causes the effective cross-sectional area for the first discs to be reduced, causing a greater radial acceleration compared to discs situated towards the aft end of the rotor. This increased radial acceleration suggests that the pressure losses for discs closer to the inlet will be greater than that for the latter and this is confirmed by the presented total pressure contour from which a total pressure loss for the first disc of 2.7% from the inlet total pressure is observed. The disc that is furthest away from the inlet has a total pressure drop of < 0.05%. Additionally, due to the aforementioned flow field developments, the mass flow rate for different disc gaps is also different. The variation in mass flow rate across the disc gaps is presented in Figure 7, together with the static pressure variation.

The entropy generation contour in Figure 6 shows a significant increase at the walls of all discs just after the interface at a radius of 13.7 [mm]. In the inlet region, the tangential Reynolds number is extremely low due to the very low tangential velocity components. However, at the interface, when the flow enters the disc gaps, the characteristic length becomes much smaller and the walls of the discs at that location are rotating relative to the tangential flow, which at that point is still almost stationary. This indicates that the relative tangential velocity (the difference in rotational speed and tangential velocity; $(\omega r - u)$ is the highest it will be for the entire rotor. The Reynolds number therefore is also highest at that location and begins to decrease from thereon. The tangential Reynolds number at that radial location reaches values of approximately 2200 (Figure 7). The subsequently increased turbulence dissipation rate causes an increase in indirect entropy generation rate. The Bejan number presented shows that the heat conduction entropy generation rate has an insignificant contribution to the total entropy generation rate which is due to the relatively low flow velocities and, more importantly, due to the high specific heat of the working fluid.

Between the radius of 19 [mm] and 28.5 [mm], the flow continues on trends previously identified at the radius range of 12.7 [mm] < r < 19 [mm]: the flow continues accelerating tangentially due to the increasing linear rotor speed as radius increases, and the radial velocity continues decreasing due to the increasing adverse pressure gradient as work is introduced to the fluid. However, in the radius range of 28.5 [mm] < r < 38 [mm], a new flow behavior appears (Figure 8).

The tangential velocity continues accelerating as a function of radius and the velocity profiles are of parabolic shape, suggesting that the tangential Reynolds number is decreasing and the flow is laminar. The radial velocity profile, however, experiences a greater than before adverse pressure gradient and as a

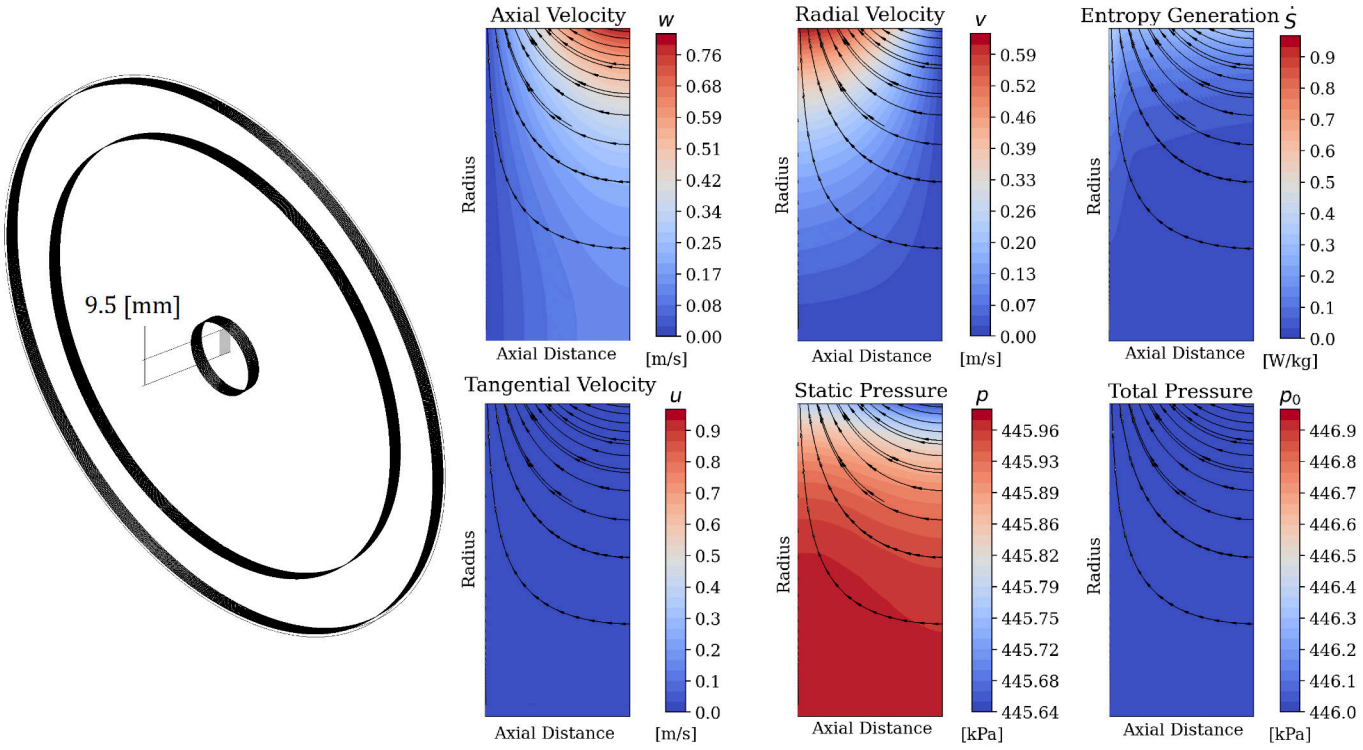


FIGURE 5: CROSS-SECTIONAL CONTOUR OF ROTOR-ONLY MODEL ALONG THE 0 DEGREE RADIAL IN THE RADIUS RANGE OF 0 [MM] < R < 9.5 [MM] (INLET REGION). PRESENTED PARAMETERS ARE AXIAL, RADIAL, TANGENTIAL VELOCITIES, TOTAL AND STATIC PRESSURE, AND ENTROPY GENERATION RATE.

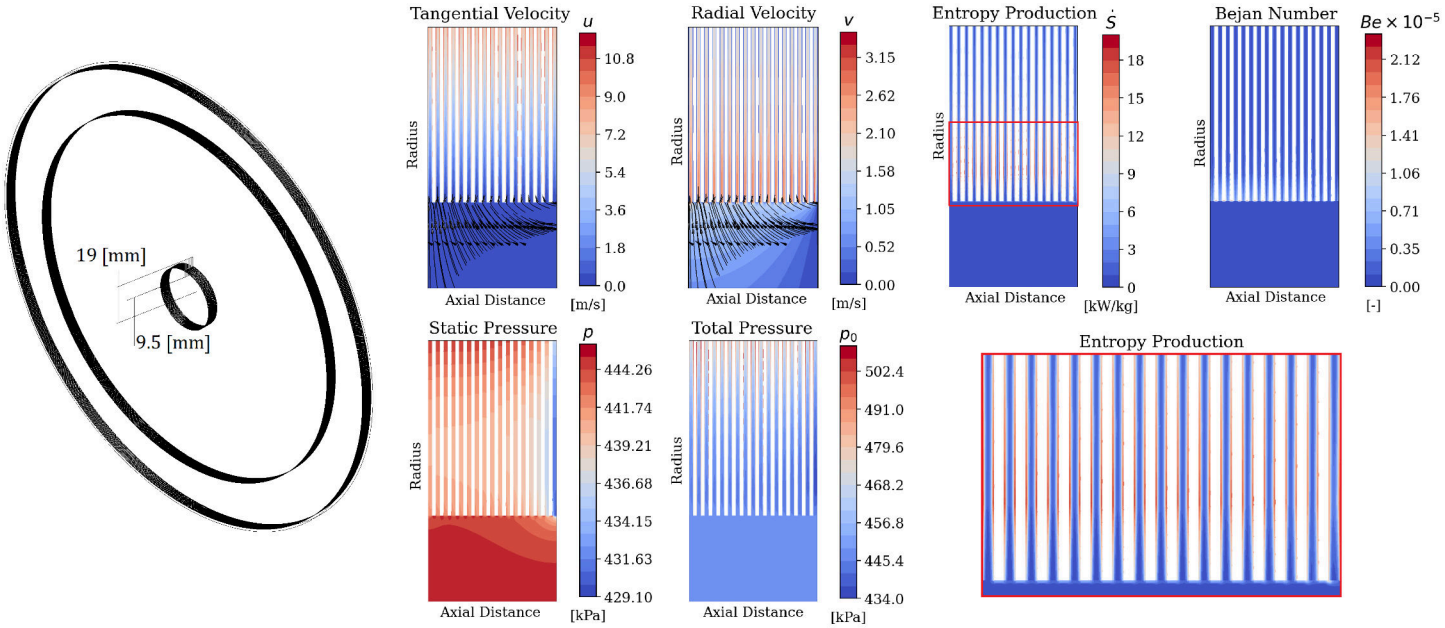


FIGURE 6: CROSS-SECTIONAL CONTOUR OF ROTOR-ONLY MODEL ALONG THE 0 DEGREE RADIAL IN THE RADIUS RANGE OF 9.5 [MM] < R < 19 [MM] (INLET INTERFACE). PRESENTED PARAMETERS ARE AXIAL, RADIAL, TANGENTIAL VELOCITIES, TOTAL AND STATIC PRESSURE, ENTROPY GENERATION RATE, AND BEJAN NUMBER.

result, the radial velocity profile begins inverting. As the examined radius increases, from the total and static pressure contours, the difference in pressure between the discs decreases from what was observed at the inlet region of the rotor with the greatest static pressure difference down to 0.8% from the previously observed 3.5%. Despite the increased adverse pressure gradient,

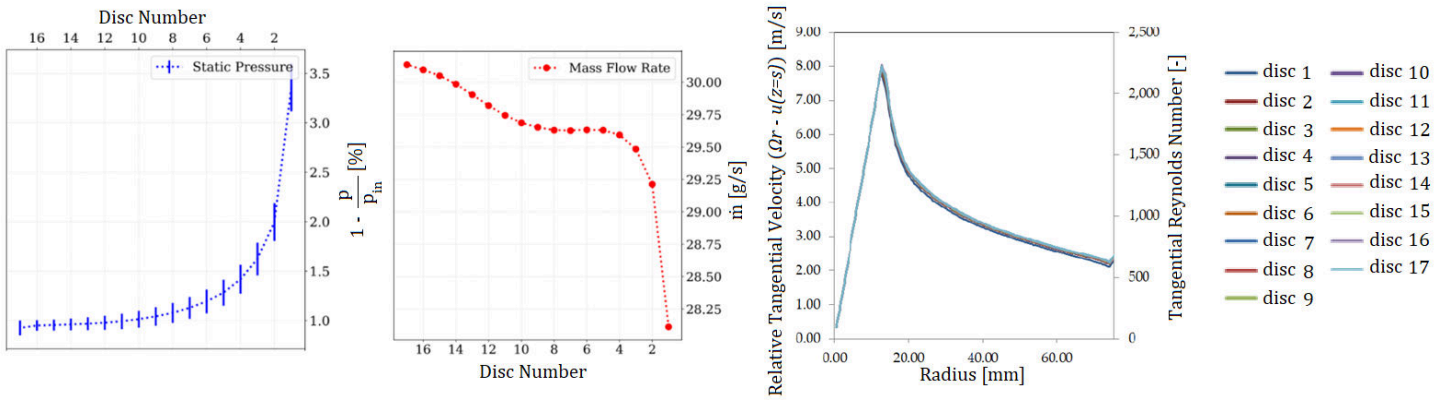


FIGURE 7: FLOW PROPERTIES AT THE INTER-DISC GAPS INTERFACING WITH THE INLET REGION. (LEFT) – STATIC PRESSURE DROP ACROSS THE INTER-DISC GAPS. (MIDDLE) – MASS FLOW RATE VARIATION ACROSS DIFFERENT INTER-DISC GAPS. (RIGHT) – RELATIVE TANGENTIAL VELOCITY AND TANGENTIAL REYNOLDS NUMBER ACROSS THE ROTOR RADIUS.

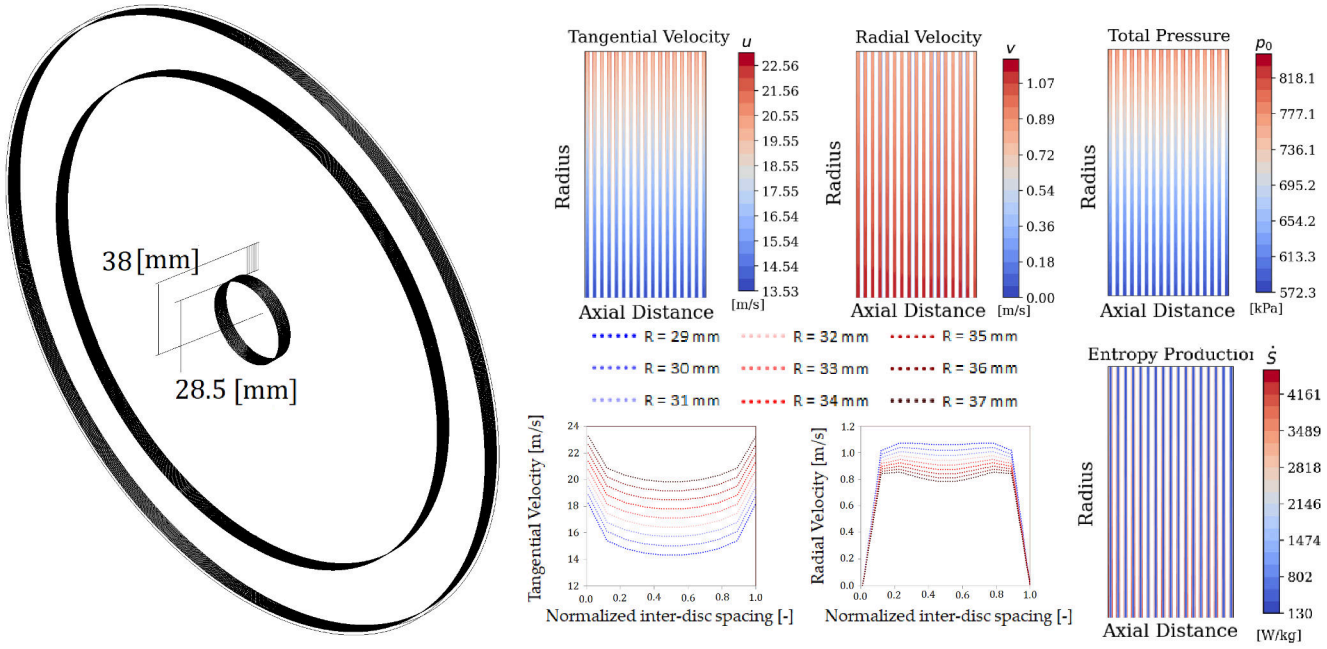


FIGURE 8: CROSS-SECTIONAL CONTOUR OF ROTOR-ONLY MODEL ALONG THE 0 DEGREE RADIAL IN THE RADIUS RANGE OF 28.5 [MM] < R < 38 [MM]. PRESENTED PARAMETERS ARE AXIAL, RADIAL, VELOCITIES AND VELOCITY PROFILES, TOTAL PRESSURE, AND ENTROPY GENERATION RATE.

the entropy generation rate is seen to continue to decrease with the increase in radius as the entropy generation rate is mainly invoked by the tangential component of the flow as opposed to the radial due to the relative tangential velocity component being an order of magnitude higher than the radial. This continues to develop in a similar fashion throughout the radius of the rotor up to the interface between the rotor and the outlet domain.

At the rotor-outlet interface (Figure 9), the flow is vented from the inter-disc gaps into the artificial outlet domain. The flow experiences a rapid tangential deceleration after it is dumped into the outlet domain, and a recirculation region is formed which is indicated by the radial velocity which is positive (positive = flows towards the outlet) towards the walls of the outlet domain and negative (negative = flows towards the discs) towards the middle of the rotor. The dump diffusion effect is also responsible for the highest observed total pressure loss at the interface of 13%. The entropy generation rate also reflects the effects of the rapidly diffused flow with a significant increase of approximately 4 orders of magnitude above what is prior to the outer interface in the rotor. The loss mechanism responsible for approximately 85% of the total entropy generation rate at the outlet domain is the turbulence dissipation rate with the remaining mostly pertaining to direct entropy generation.

The performance of the rotor from the rotor-only model is presented in Figure 10. The total pressure ratio of each disc in the rotor assembly is similar with variation in pressure ratio of ±

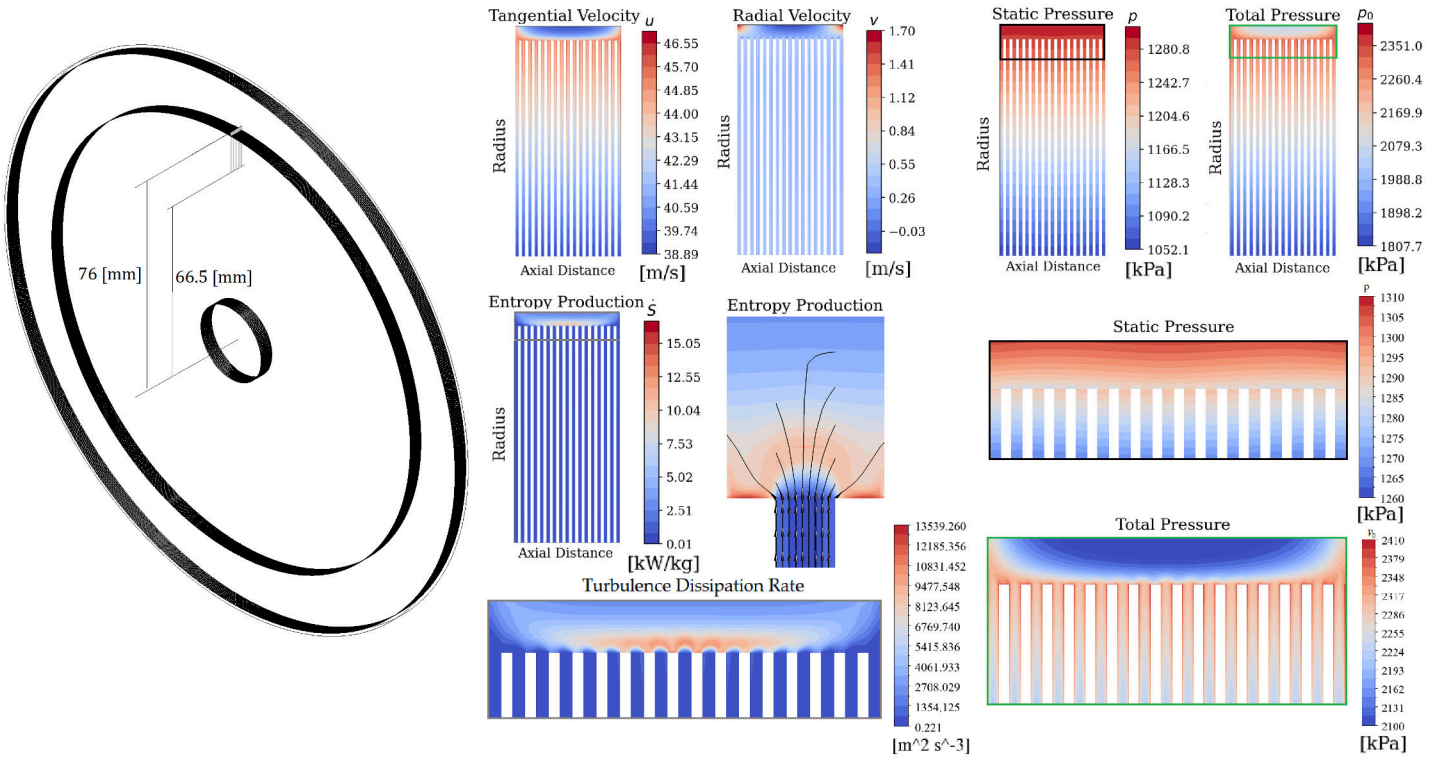


FIGURE 9: CROSS-SECTIONAL CONTOUR OF ROTOR-ONLY MODEL ALONG THE 0 DEGREE RADIAL IN THE RADIUS RANGE OF 66.5 [MM] < R < 76 [MM]. PRESENTED PARAMETERS ARE AXIAL, RADIAL, VELOCITIES, TOTAL AND STATIC PRESSURE, ENTROPY GENERATION RATE, AND TURBULENCE DISSIPATION RATE.

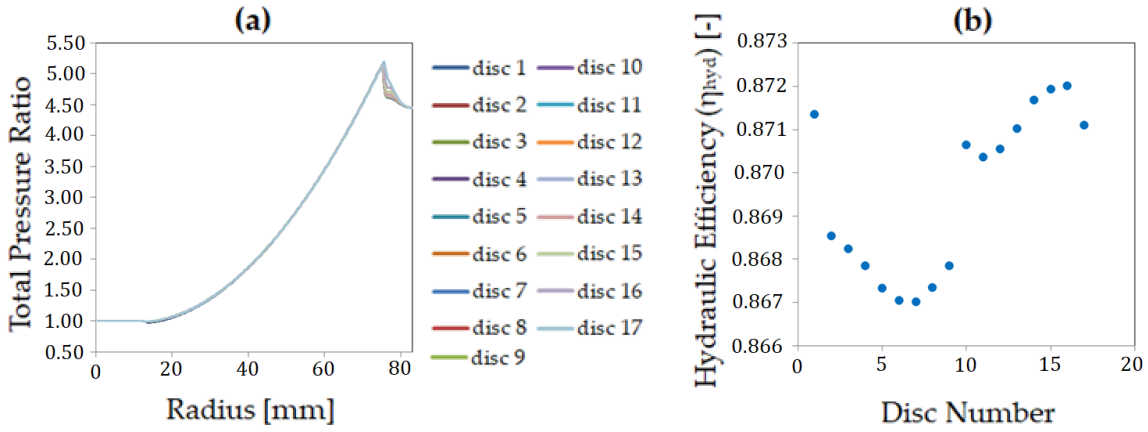


FIGURE 10: ROTOR TOTAL PRESSURE RATIO (A) AGAINST PUMP RADIUS FOR EACH INTER-DISC GAP OF THE ROTOR-ONLY MODEL. ROTOR HYDRAULIC EFFICIENCY OF ROTOR-ONLY MODEL (B) FOR EACH INTER-DISC GAP.

0.03 which is nearly uniform and the differences are within the numerical resolution of the model. Therefore, it can be concluded that the total pressure ratio for all inter-disc gaps for this model is nearly uniform at 5.2 [-]. Similarly, the hydraulic efficiency (Equation 8) exhibits a variation across the discs of ± 0.5% which is again nearly uniform and within the numerical resolution of the model. Therefore, the overall hydraulic efficiency – calculated between the inlet of the model and outlet of the rotor for this model – is estimated to be 87%. This finding is in line with previous studies, which state that the efficiency of the rotor in a boundary layer pump is high compared to the overall pump efficiency. Despite this, the areas of highest loss in a boundary layer pump rotor are at the inner rotor interface of the pump where the flow is diverted and contracted into the rotor assembly and at the outlet of the rotor – where the flow is dumped causing a significant loss in total pressure and an increase in turbulence dissipation rate. In the above discussion, all cross-sections are taken at the 0 degree radial (12 o'clock) and in Figure 11, it is shown that is unnecessary to examine other radials in detail for this particular model as the flow development is shown to be axially symmetric to a very high degree. The only instance in which an asymmetric event is observed is in the outlet domain,

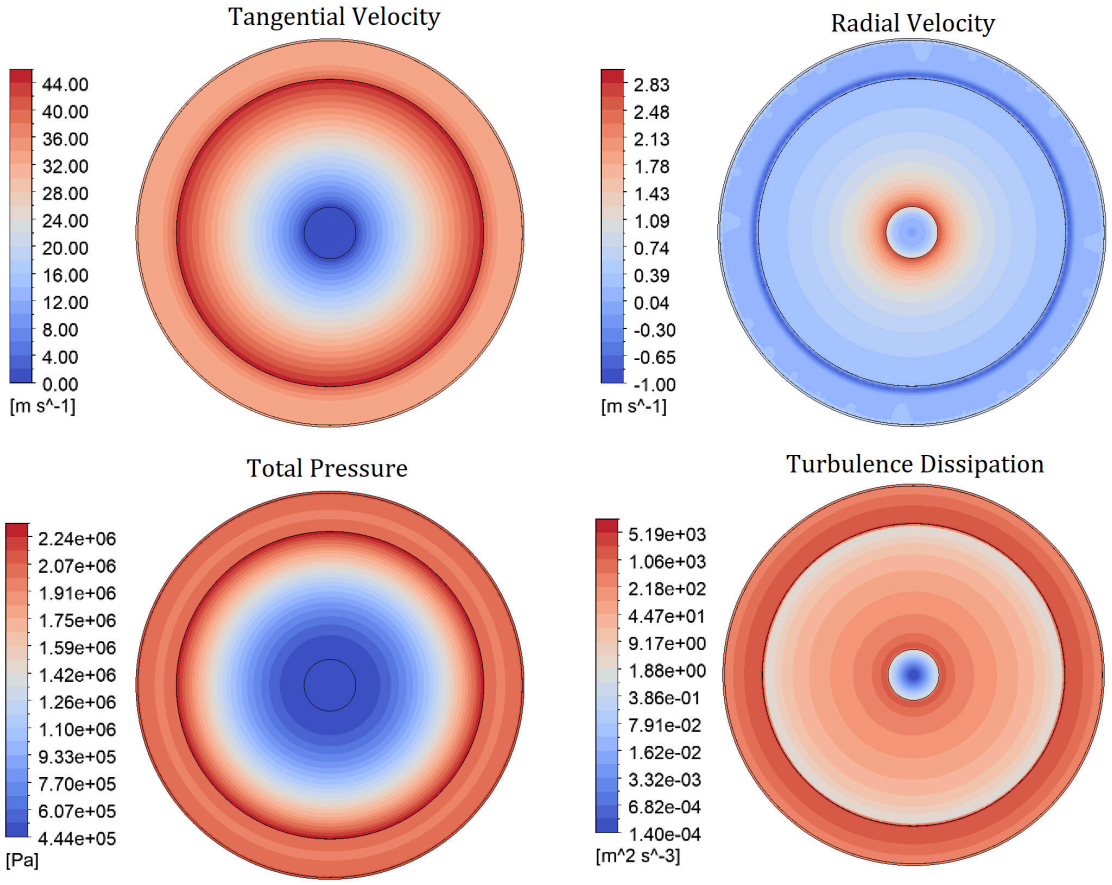


FIGURE 11: CROSS-SECTIONAL VIEW AT HALF-THICKNESS OF THE ROTOR IN THE ROTOR-ONLY MODEL.

where the radial velocity experiences a variation as a function of the circumferential direction. But since this domain is artificially added for computational reasons, further investigation of the flow developments in that location is not necessary.

$$\eta_{hyd} = \frac{Q(p_{0_2} - p_{0_1})}{J\omega} \tag{8}$$

3.2 Volute-only Model

The volute-only model results serve the purpose of obtaining the efficiency of the volute geometry without the results being affected by integration related concerns like secondary flow features generated by back pressure propagation. In this section, the cylindrical velocity components, total pressure, and entropy generation in the volute channel are examined as presented in Figure 12. It is worth reiterating that Stepanoff's method is supposed to design volute geometries with constant kinetic energy; i.e., the radial velocity is assumed zero, and the tangential velocity is constant. Furthermore, the volute inlet is initialized with the rotor outlet conditions from the rotor-only simulation. The results presented in Figure 12 confirm that the velocity vector mainly consists of tangential velocity, however, the tangential velocity is not constant as a tangential acceleration is observed as a function of the tangential angle. This is due to the volute tongue which creates an area contraction in which the flow accelerates. In the region of the volute channel in close proximity to the volute tongue, the entropy generation rate is increased significantly due to the higher velocities and frictional forces causing both high direct and indirect entropy production. The increase in total entropy production is observed to be 2 orders of magnitude higher that what was seen anywhere in the rotor-only simulation. Despite the increased entropy generation rates, however, these regions are very localized, indicating that the performance of the volute is not affected significantly by this. The calculated hydraulic efficiency (Equation 8) of the volute based on the simulation results is 97.3%.

3.3 Integrated Model

In the integrated model, the flow enters the inlet domain identically to the rotor-only model. The flow then diverts to each disc gap as seen previously. In the integrated model however, the resulting losses due to this process are proportionally higher due to the increased number of discs. Examining the radial velocity in Figure 13 reveals that contrary to the baseline rotor-only model, discs closer to the inlet and the back wall of the pump experience fully reversed flow as indicated by the negative radial velocities. Furthermore, the flow tends to favor the path through the 180 degree radial than the 0 degree radial – where the volute tongue is – as indicated by the asymmetry observed in the inlet region. The tangential velocity magnitudes are similar to those of the baseline rotor-only model and therefore, the entropy generation rate at the inlet region and the interface is within the same order

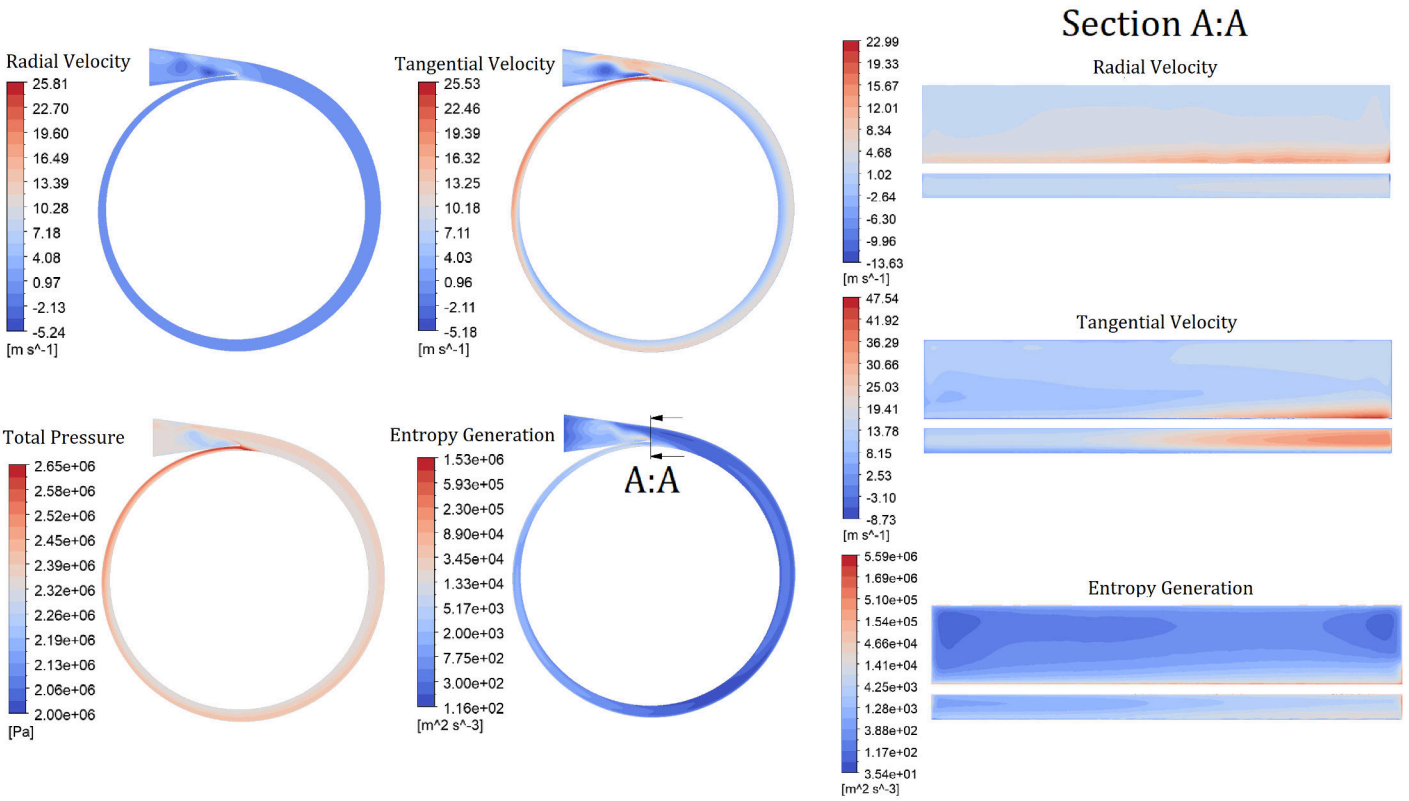


FIGURE 12: FLOW FIELD RESULTS FROM VOLUTE-ONLY MODEL. PRESENTED PARAMETERS ARE RADIAL AND TANGENTIAL VELOCITY, TOTAL PRESSURE, AND ENTROPY GENERATION. A CROSS-SECTIONAL VIEW AT THE VOLUTE TONGUE IS ALSO PRESENTED.

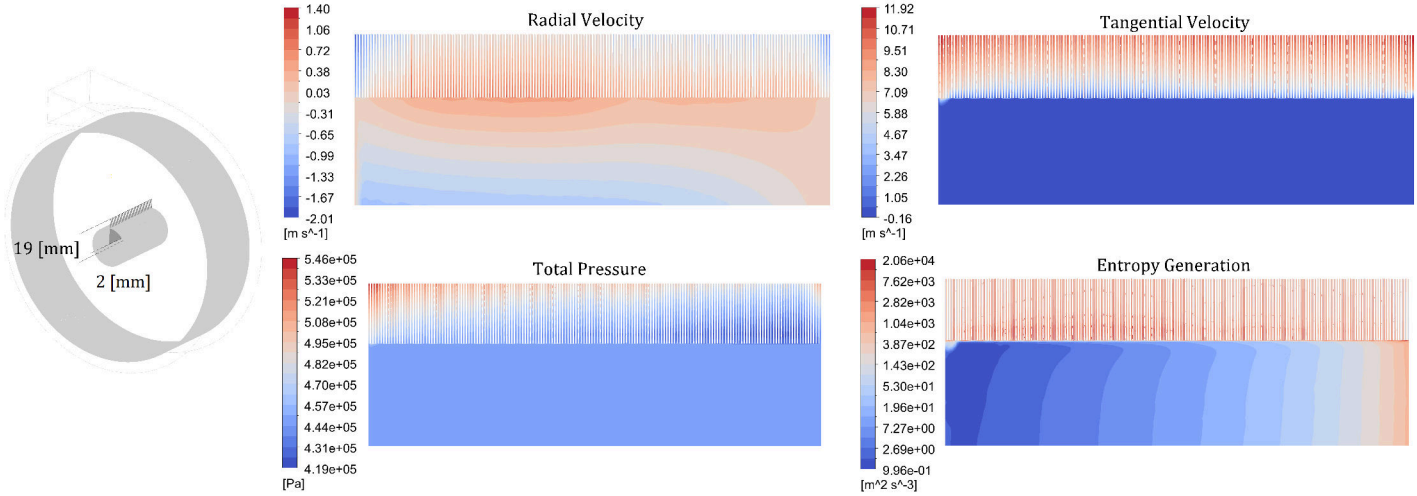


FIGURE 13: CROSS-SECTIONAL CONTOUR OF INTEGRATED MODEL ALONG THE 0 DEGREE RADIAL IN THE RADIUS RANGE OF 2 [MM] < R < 19 [MM]. PRESENTED PARAMETERS ARE RADIAL AND TANGENTIAL VELOCITIES, TOTAL PRESSURE, AND ENTROPY GENERATION RATE.

of magnitude as that of the baseline model. However, in the integrated case, a much greater volume is affected by higher entropy generation rates due to the reversed radial flows which result in greater losses. These losses are quantified by the total pressure contour which reveals that the greatest total pressure drop, occurring at the disc gap closest to the inlet, is 6% from the inlet total condition which is more than twice the total pressure drop at the inlet of the baseline rotor-only case.

As the flow develops, the negative radial velocity at the cross section in Figure 14 indicates that the flow is entirely reversed and the relative tangential velocity is also negative above radius of 41 [mm], which indicates that the flow is imposing a force onto the discs instead of the opposite. This concludes that this tangential section of the pump's rotor does not contribute to the

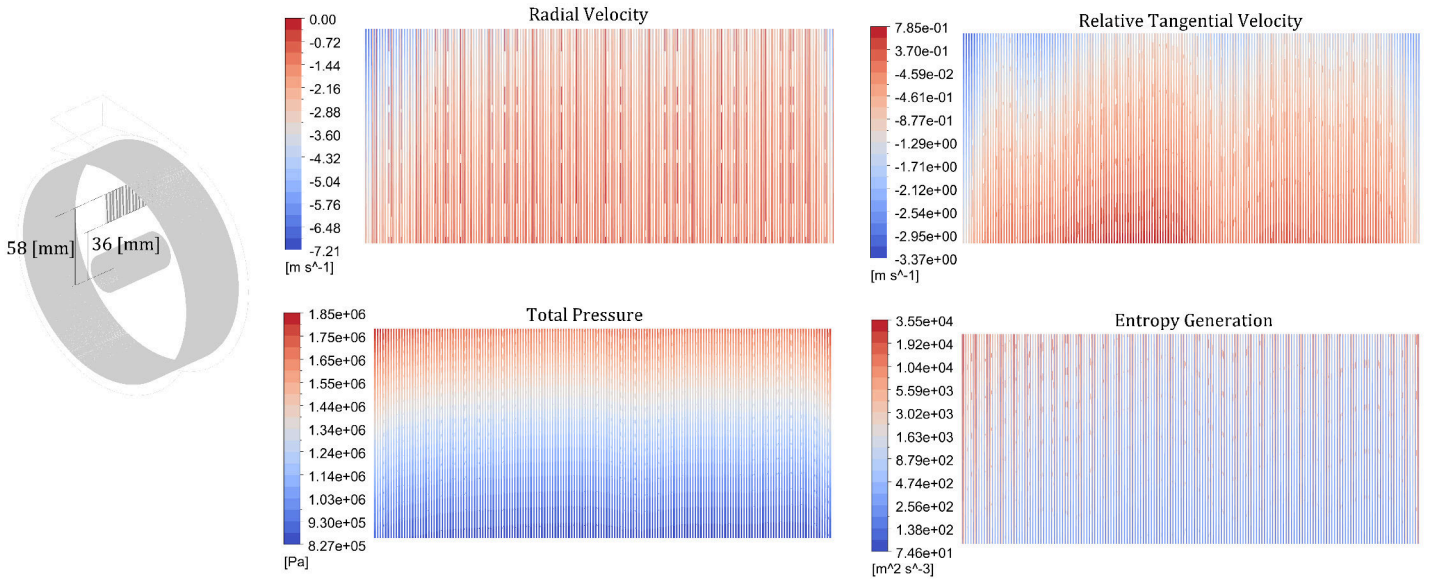


FIGURE 14: CROSS-SECTIONAL CONTOUR OF INTEGRATED MODEL ALONG THE 0 DEGREE RADIAL IN THE RADIUS RANGE OF 36 [MM] < R < 58 [MM]. PRESENTED PARAMETERS ARE RADIAL AND RELATIVE TANGENTIAL VELOCITIES, TOTAL PRESSURE, AND ENTROPY GENERATION RATE.

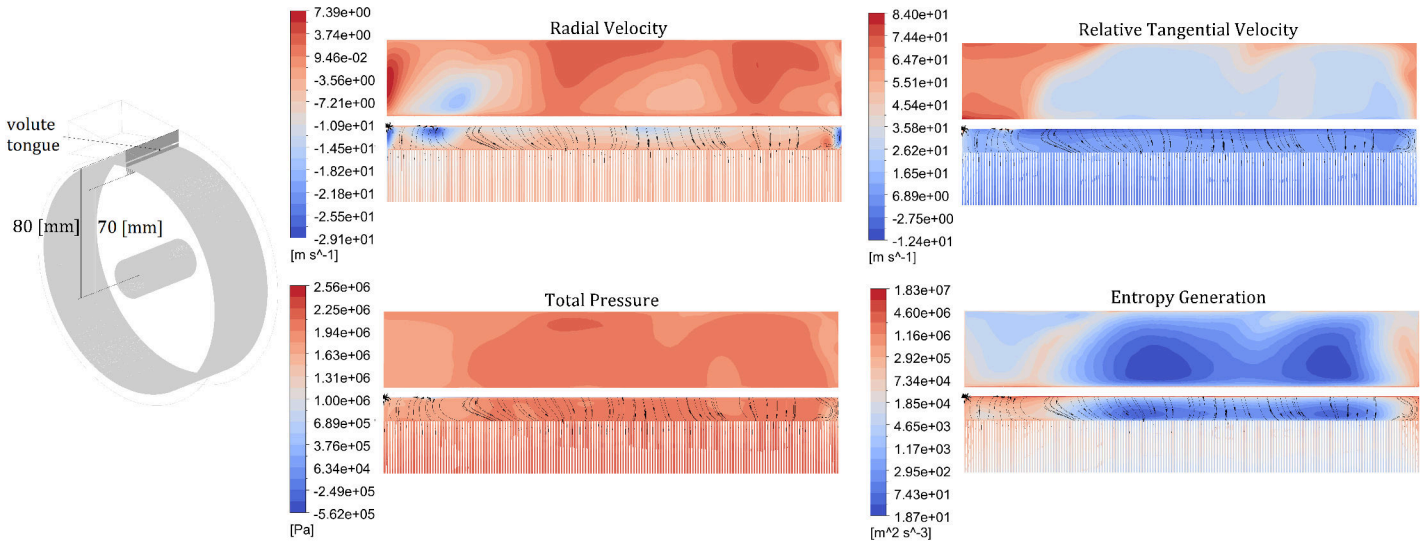


FIGURE 15: CROSS-SECTIONAL CONTOUR OF INTEGRATED MODEL ALONG THE 0 DEGREE RADIAL IN THE RADIUS RANGE OF 70 [MM] < R < 87 [MM] (ROTOR-VOLUTE INTERFACE UNDERNEATH VOLUTE TONGUE). PRESENTED PARAMETERS ARE RADIAL AND RELATIVE TANGENTIAL VELOCITIES, TOTAL PRESSURE, AND ENTROPY GENERATION RATE.

overall work done on the fluid and that it only contributes to losses. Where the flow experiences the highest negative radial and relative tangential components, the entropy generation rate is highest. At this cross-section, the entropy generation rate reaches magnitudes that are higher than those observed at the inlet region; an event previously unseen with the baseline model.

At the interface between the rotor and the volute outlet channel (Figure 15), the root cause of the previously observed reversed flows is seen. At the tongue, the flow is split, causing a significant negative radial velocity component and is imposed onto the flow inside the rotor, adding an additional force towards the inlet causing the flow to separate from the disc wall. The relative tangential velocity magnitude in the rotor assembly leading to the interface is small compared to that of the rotor-only model and for the first and last discs in the rotor pack, the magnitude is negative. The total pressure at the interface underneath the volute tongue does not present a significant pressure drop as observed in the rotor-only model because there is no dump diffusion due to the smaller volume change; however, the total pressure at the interface for the integrated model is approximately 15% lower than that of the rotor-only model at the same location. The entropy generation rate at the fore and aft discs of the rotor assembly and in the volute channel underneath the tongue is 3 orders of magnitude higher than that observed in any other location of the integrated

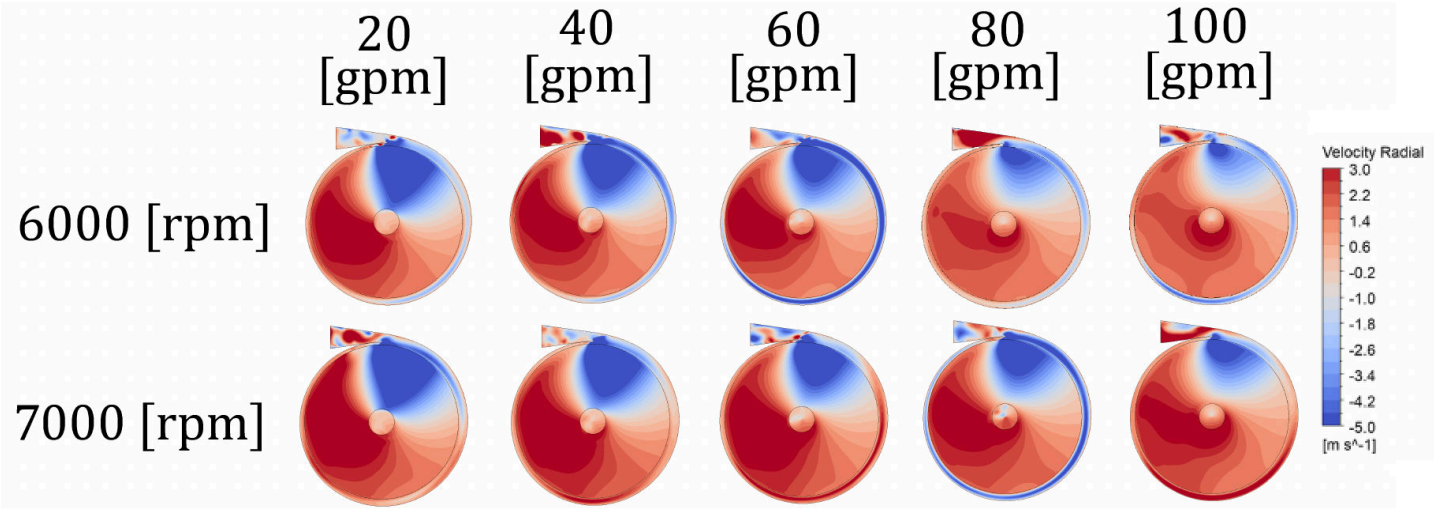


FIGURE 16: RADIAL VELOCITY CONTOURS AT HALF-THICKNESS OF THE INTEGRATED MODEL FOR 5 DIFFERENT MASS FLOW RATES AND 2 ROTATIONAL SPEEDS.

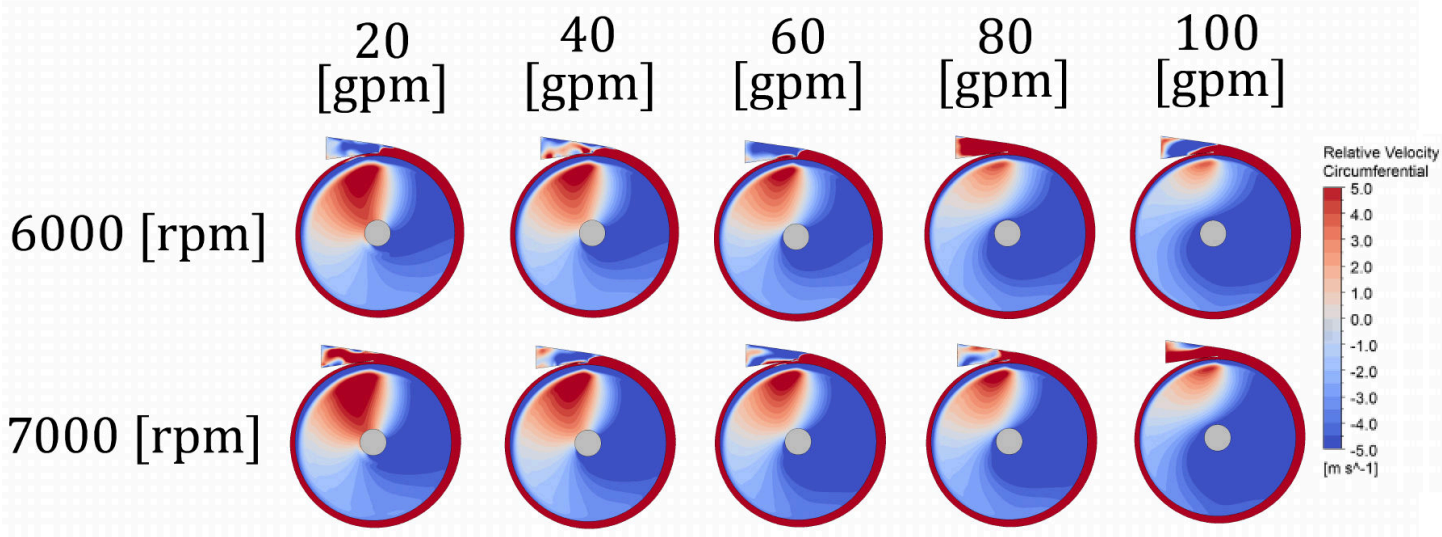


FIGURE 17: TANGENTIAL VELOCITY CONTOURS AT HALF-THICKNESS OF THE INTEGRATED MODEL FOR 5 DIFFERENT MASS FLOW RATES AND 2 ROTATIONAL SPEEDS.

model and the rotor-only model. The increased losses are due to the higher velocity magnitudes near the volute walls and corners, particularly around the volute tongue.

To examine the aforementioned flow developments for the design point case in different tangential locations, Figure 16 and Figure 17 (6000 [rpm], 80 [gpm] – design point conditions) present a side-view of the radial and tangential velocity distribution around the axis of rotation. The reversed radial flow is shown by the negative radial velocities which are highest at the 0 degree radial – just under the volute tongue – and the magnitude decreases closer to the inlet at that radial. Because of this, however, the desired mass flow rate at the outlet must be achieved, therefore observing higher radial velocities at the 270 and 180 degree radials which are compensating for the issues caused by the volute tongue. Because of the effects of the tongue on the rotor, the relative tangential velocity near the tongue is positive, which means that the tangential velocity is faster than the disc speed ($u - \omega r$), indicating that the flow is imposing a frictional force onto the disc as opposed to what is desired. Radial sections of the rotor in which the tangential velocity is higher than the disc speed only contribute to losses as seen in the entropy generation side-view contour in Figure 18. In regions of the entropy generation contour where the relative tangential velocity is greater than 0 (i.e., ahead of the disc) the entropy generation rate is highest. At locations where the relative tangential velocity is below 0, the entropy generation rate is still high because of losses introduced by friction in both the radial and tangential direction. At locations where the relative tangential velocity is close to zero, the entropy generation rate decreases drastically as there no longer is tangential friction, only radial.

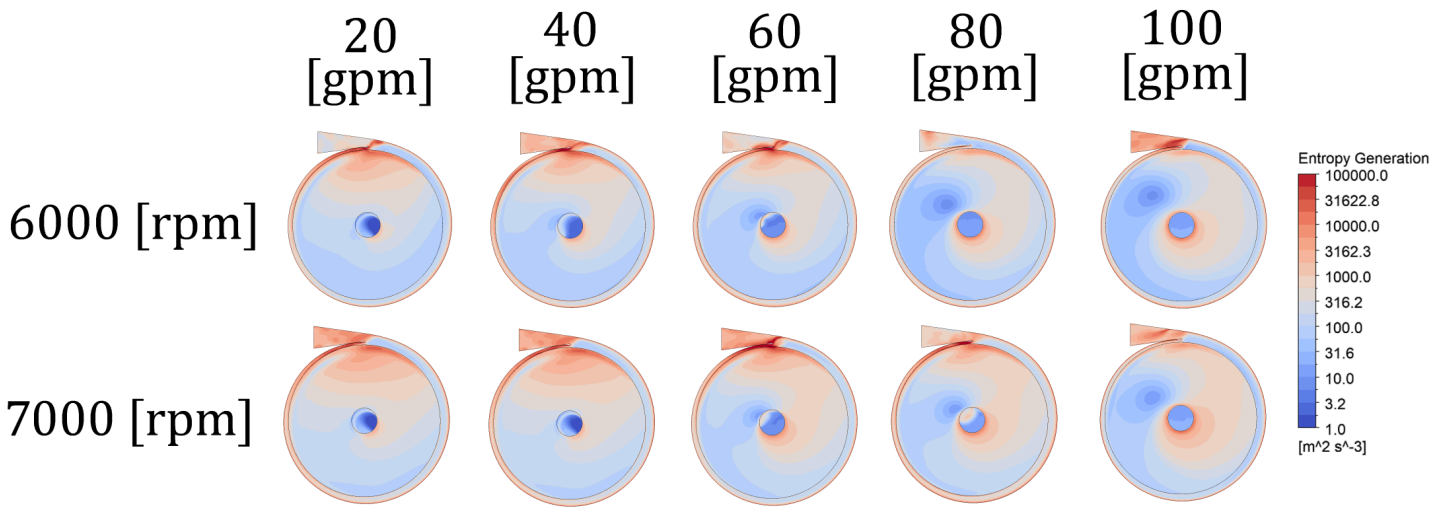


FIGURE 18: ENTROPY GENERATION CONTOURS AT HALF-THICKNESS OF THE INTEGRATED MODEL FOR 5 DIFFERENT MASS FLOW RATES AND 2 ROTATIONAL SPEEDS.

3.4 Integrated Pump Off-Design Results

Examining Figures 16 and 17 once more shows how different flow rates and rotational speeds affect the aforementioned flow developments. The reversed radial flow is seen to be highest at low flow rates (and thus high pressure ratios) and lowest at high flow rates. Comparing between the two examined rotational speeds, the reversed flow magnitude is greater for greater rotational speeds. The performance of the pump is confirmed to be increased with reduction in reversed radial flow by examining the relative tangential velocity ($u - \omega r$) where positive values indicate that the flow is posing a frictional force on the discs (flow is *ahead* of disc – undesirable) and negative – the disc is posing a frictional force on the flow (flow is *behind* of disc). With increasing flow rates, the rotor area affected by adverse tangential flows reduces, therefore reducing the entropy production rates displayed in Figure 18.

In Figure 19, the hydraulic efficiency and pressure ratio from the present study and the experimental results are plotted. It is observed that generally, good agreement between the CFD and experimental results is observed. At low flow rates, the discrepancies are lower with the lowest error being 3.9%. The errors increase nearly linearly to a maximum value of 39.1% at the highest examined flow rate. The observed difference is mainly due to features that are not included in the model such as leakage losses, friction between the rotor and casing through seals, and the lack of disc spacers in the model. Moreover, given the somewhat limited information on how the experiment was conducted, experimental error may also be a significant factor to the discrepancy. Morris [13] has reported the location and accuracy of the used measurement equipment for the experiment. One probe is of greater concern than the rest which is a pitot-static tube placed tangentially to the rotor outlet in attempt to measure and capture the rotor performance. However, due to the very small inter-disc gaps, it is estimated that the effect of the pitot-static tube on the flow is not negligible and therefore the calculated by Morris rotor performance results are not used in this study. The reported by Morris [13] tolerances for the pressure measurements at the inlet and outlet of the pump are approximately ±2% for both. The reported measurement error of torque and speed is ± 1% [13]. These uncertainties combined can results in the maximum possible error in hydraulic efficiency of 3.8% at the design point. Nevertheless, the agreement between theoretical and experimental data is satisfactory considering past studies performing similar analyses in the available literature [7, 8, 28]. The comparison of pressure ratios again show a difference between CFD and experimental results, however, in this case the variation is more consistent between 6% and 10%, which is to confirm once again that the errors are due to not modeled features and that 3D RANS solutions are the adequate approach to a theoretical study of a boundary layer pump.

3.5 Potential Optimization Strategy

The more reasonable approach to improving the efficiency of a boundary layer pump is to implement modifications to the volute outlet channel instead of the rotor because the advantages of boundary layer pumps are mainly due to the simplistic design of the rotor. Furthermore, the presented results in the previous sections support that the efficiency of the rotor in the integrated pump model is 2.5 times higher than that of the entire pump, definitively concluding the need for a better-designed volute. The investigation of the flow field in the integrated pump model concluded that a significant loss in rotor efficiency is caused under the volute tongue which splits the flow and causes an inverse radial velocity component with a large magnitude. This flow is responsible for the flow separation in the rotor, suggesting that the efficiency of the rotor, and therefore the overall pump, may be improved if the volute tongue is radially further away from the rotor outlet. Increasing the gap size of a volute is a common practice for centrifugal compressor and has been done for boundary layer pumps, but with minimal elaborations in reference [8]. To investigate this further, two new volute geometries are developed. The first one having a volute tongue gap of 5 times that of the original volute (12.5 [mm]) and the second – 10 times the gap (25 [mm]). The domain discretization methodology and computational setup of

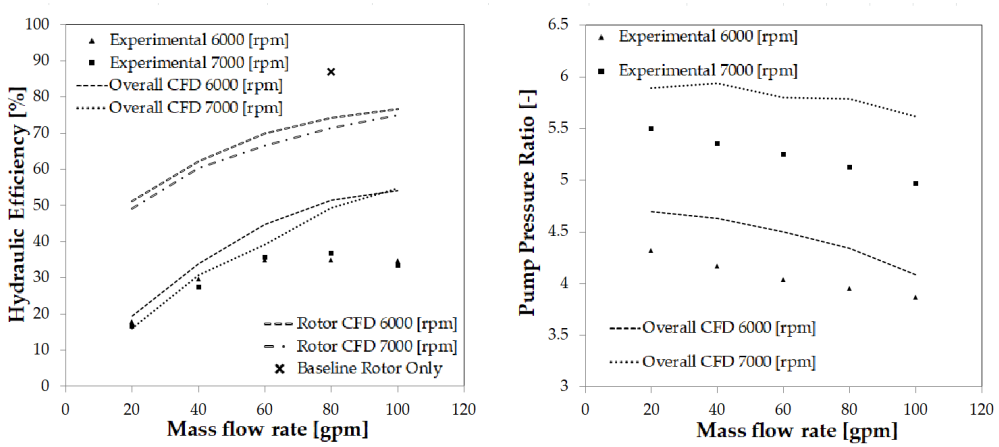


FIGURE 19: HYDRAULIC EFFICIENCY (LEFT) FOR OVERALL PUMP EXPERIMENTAL AND CFD RESULTS AND FOR CFD RESULTS FROM INTEGRATED MODEL ACROSS THE ROTOR. PRESSURE RATIO (RIGHT) FOR EXPERIMENTAL AND CFD RESULTS FOR THE OVERALL PUMP.

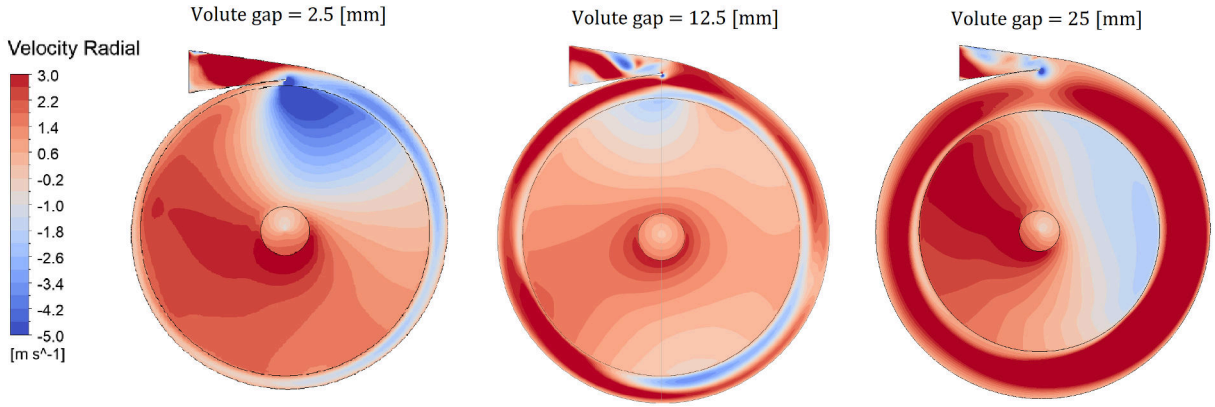


FIGURE 20: SECTION VIEW OF RADIAL VELOCITY AT HALF-THICKNESS OF THREE BOUNDARY LAYER PUMPS WITH DIFFERENT VOLUTE TONGUE GAP CLEARANCES

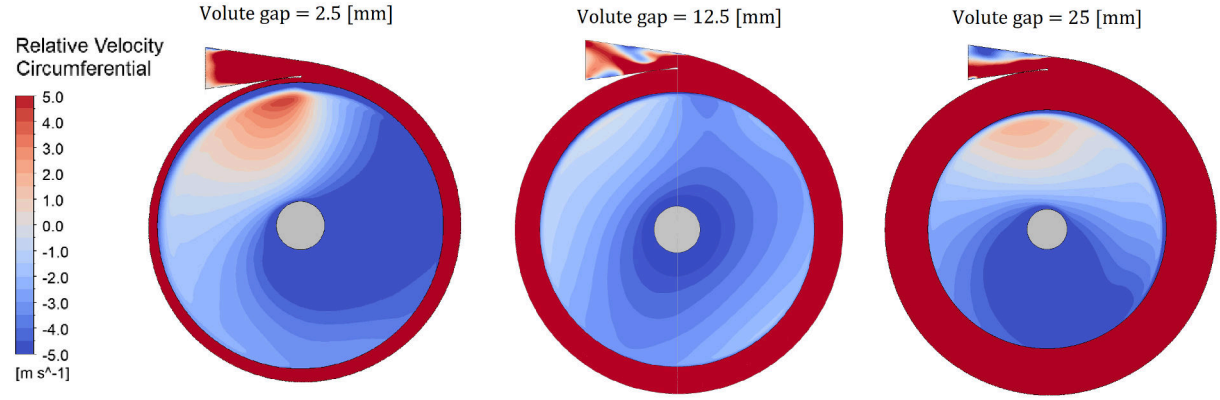


FIGURE 21: SECTION VIEW OF RELATIVE TANGENTIAL VELOCITY AT HALF-THICKNESS OF THREE BOUNDARY LAYER PUMPS WITH DIFFERENT VOLUTE TONGUE GAP CLEARANCES

these two new volutes is identical to that of the original volute and integrated pump model. The two new integrated pump models with the new volutes are run at 6000 [rpm], 80 [gpm] (design point condition).

In Figures 20, 21, 22, a cross-sectional view in the middle of the three pumps are presented, showing the flow field development in terms of radial velocity, relative tangential velocity, and entropy generation rate respectively. Increasing the volute gap

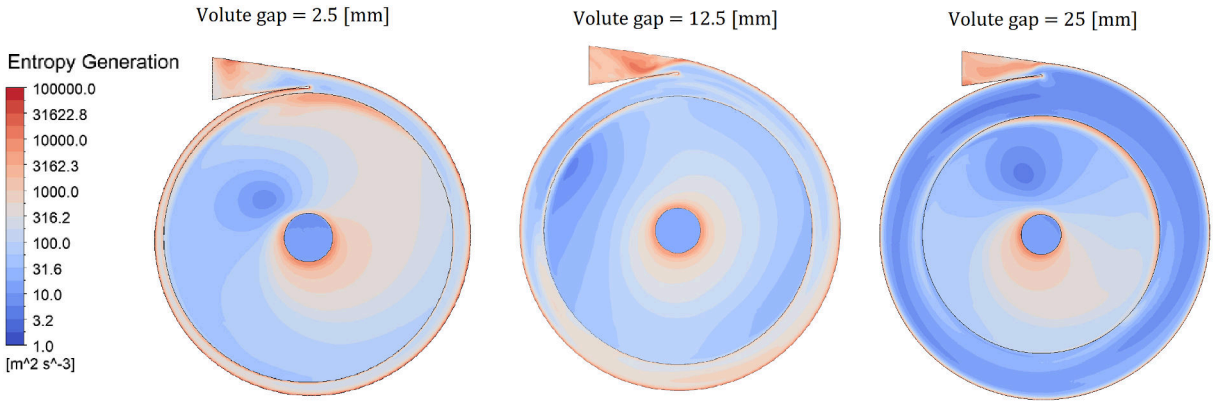


FIGURE 22: SECTION VIEW OF ENTROPY GENERATION RATE AT HALF-THICKNESS OF THREE BOUNDARY LAYER PUMPS WITH DIFFERENT VOLUTE TONGUE GAP CLEARANCES

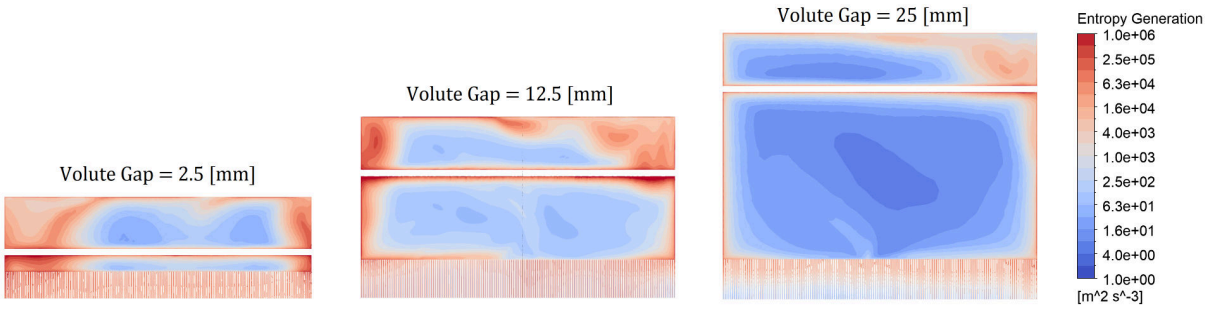


FIGURE 23: SECTION VIEW OF ENTROPY GENERATION RATE ALONG THE ZERO-DEGREE RADIAL AT THE INTERFACE BETWEEN THE ROTOR AND VOLUTE FOR THREE BOUNDARY LAYER PUMPS WITH DIFFERENT VOLUTE TONGUE GAP CLEARANCES

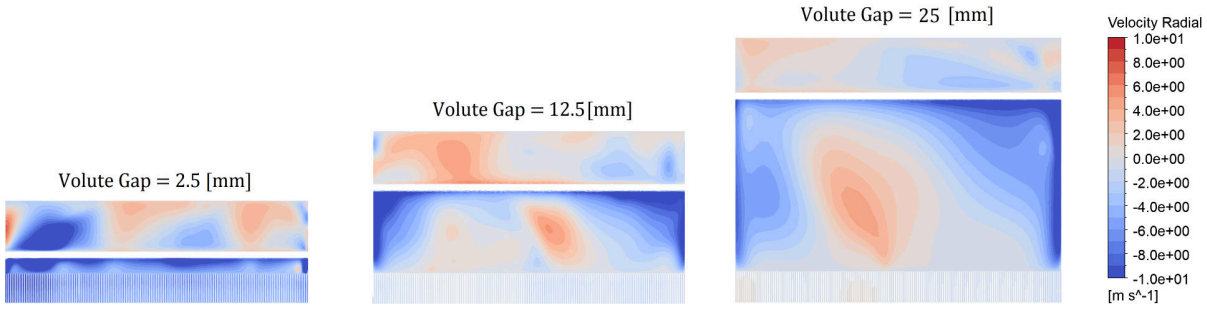


FIGURE 24: SECTION VIEW OF RADIAL VELOCITY ALONG THE ZERO-DEGREE RADIAL AT THE INTERFACE BETWEEN THE ROTOR AND VOLUTE FOR THREE BOUNDARY LAYER PUMPS WITH DIFFERENT VOLUTE TONGUE GAP CLEARANCES

to 12.5 [mm] shows the greatest improvement in the rotor's flow field. Compared to the original volute with a gap of 2.5 [mm], the negative radial velocity regions are now limited to a significantly smaller portion of the rotor than seen previously. Furthermore, the relative tangential velocity contour for the pump with a volute gap of 12.5 [mm] shows no positive relative tangential velocities in the rotor, indicating that in all regions of this cross-sectional view of the rotor there is no friction imposed by the fluid onto the rotor walls. Following these improvements in the flow field for the 12.5 [mm] volute gap model, a significant reduction in entropy generation rate is observed in the rotor within the radius range $25[mm] < r < 75[mm]$. Increasing the gap further from 12.5 [mm] up to 25 [mm] leads to worsening of the flow field properties as the region with negative radial velocity in the rotor now increasing in area and observing a positive relative tangential velocity component under the volute tongue once again – similar to the original volute. Entropy generation rate is also noted to rise for the largest gap volute in multiple locations – at the rotor outlet under the tongue and at the 180-degree radial. With a greater volute gap, the cross-sectional area of the volute becomes larger allowing for greater static pressure recovery which then imposes a larger adverse pressure gradient onto the rotor. It can, there-

fore, be concluded that increasing the volute gap is a trade-off between the large negative fluxes caused by the volute tongue and the increasing pressure recovery due to a larger volute.

In Figures 23 and 24 a cross-sectional view at the interface between the rotor and outlet, at the volute tongue is presented showing the radial velocity and entropy generation rate. The decrease in negative radial velocity components at the interface is clearly seen between the three volutes and the reduction in entropy generation rate at the tongue region is also apparent. Despite that the greatest rotor efficiency is obtained with the volute gap of 12.5 [mm], the entropy generation caused by the corners and walls of that volute is still great compare to the 25 [mm] gap volute. This indicates that further optimization strategies must be included for the volute geometry in order to increase the rotor efficiency but also to minimize losses in the volute.

Lastly, a summary of the flow field discussions is provided in Figure 25 in the form of a graph, depicting the efficiency changes for the pump models with different volutes against volute tongue gap clearances. Both the rotor and overall pump efficiencies change proportionally for a given volute tongue gap clearance and the parabolic tendency of the efficiency against the volute gap size is evident.

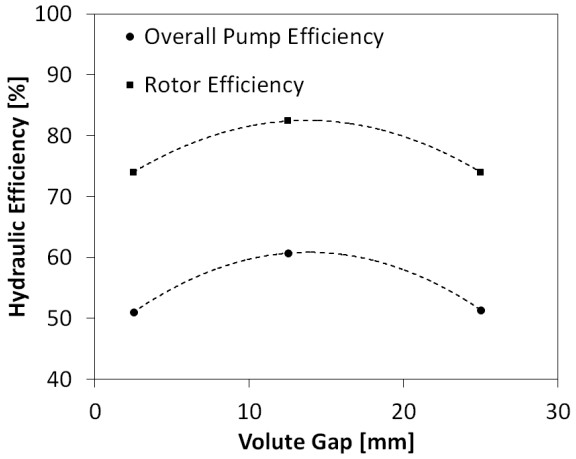


FIGURE 25: CFD RESULTS OF HYDRAULIC EFFICIENCY OF BOUNDARY LAYER PUMP MODELS AGAINST VOLUTE TONGUE GAP CLEARANCE.

4. CONCLUSION

This study performed a high-fidelity, 3D RANS solution of an experimentally tested boundary layer water pump. Three distinct models are created: a baseline rotor-only model designed to assess the rotor performance without it interacting with the volute outlet; a volute-only model to assess its performance without it interacting with the rotor; and finally, an integrated model consisting from both the rotor assembly and a volute outlet channel. It is concluded:

- The baseline rotor-only model confirms that the efficiency of the rotor in a boundary layer pump is in fact satisfactory. Areas of higher entropy generation rate were discovered in the inlet region and outlet region of the rotor due to contraction and diffusion of the flow. Nevertheless, the rotor performance without it interacting with the volute is assessed to be 87%.

- The volute-only simulation revealed that the volute geometry alone is efficient with hydraulic efficiencies of approximately 97% despite observing higher entropy generation rates around the corners of the volute cross section and in close proximity to the volute tongue. It is seen, however, that the typically observed experimental efficiencies of boundary layer pumps are not comparable to the two models being examined separately.

- To examine the interaction between the rotor and volute, a parametric sweep of the integrated model is performed over mass flow rate and rotational speed, which demonstrated that a great portion of the flow in the rotor is reversed due to the volute tongue splitting the flow and directing it towards the rotor center. This is seen to cause complete flow separation at large sections of the rotor which only contribute to losses as the tangential velocity in those regions is faster than the disc speed.

- The integrated case shows good agreement with the experimental data with trends that agree with what was reported by Wang et al. in 2014 [7] – at lower flow rates the agreement is better than at higher flow rates. This is considered to be due to features in the model that were not modeled, which introduce leakage and frictional losses.

- The results and flow field insights in this study, combined with the efficiency gains obtained from the preliminary mitigation strategy, provide directions regarding the design development of boundary layer pumps to surpass the typically quoted overall pump efficiency limits of 60%.

ACKNOWLEDGMENTS

A great thanks to Steve Brown for the comments and support on this study.

REFERENCES

[1] Armstrong, J. H. "An Investigation of the Performance of a Modified Tesla Turbine." Thesis, Georgia Institute of Technology. 1952.

[2] Rice, Warren. "An analytical and experimental investigation of multiple disk pumps and compressors." *Journal of Engineering for Gas Turbines and Power* Vol. 85 No. 3 (1963): pp. 191–198. DOI 10.1115/1.3675253.

[3] Ji, F., Bao, Y., Zhou, Y., Du, F., Zhu, H., Zhao, S., Li, G., Zhu, X. and Ding, S. "Investigation on performance and implementation of Tesla turbine in engine waste heat recovery." *Energy Conversion and Management* Vol. 179 (2019). DOI https://doi.org/10.1016/j.enconman.2018.10.071.

[4] Heng, Yaguang, Han, Yuming, Zhang, Huiyu, Zhang, Weibin, Bois, G, Jiang, Qifeng, Wang, Zhengwei and Liu, Xiaobing. "Tesla Bladed Pump (Disc Bladed Pump) Preliminary Experimental Performance Analysis." *Energies* Vol. 13 (2020). DOI http://dx.doi.org/10.3390/en13184873.

[5] Talluri, L., Dumont, O., Manfrida, G., Lemort, V. and Fiaschi, D. "Experimental investigation of an Organic Rankine Cycle Tesla turbine working with R1233zd(E)." *Applied Thermal Engineering* Vol. 174 (2020). DOI https://doi.org/10.1016/j.applthermaleng.2020.115293.

[6] Galindo, Yovany, Reyes-Nava, Juan A., Hernández, Yanhsy, Ibáñez, Guillermo, Moreira-Acosta, Joel and Beltrán, Alberto. "Effect of disc spacing and pressure flow on a modifiable Tesla turbine: Experimental and numerical analysis." *Applied Thermal Engineering* Vol. 192 (2021): p. 116792. DOI 10.1016/j.applthermaleng.2021.116792. URL https://linkinghub.elsevier.com/retrieve/pii/S1359431121002453.

[7] Wang, Baotong, Okamoto, Koji, Yamaguchi, Kazuo and Teramoto, Susumu. "Loss mechanisms in shear-force pump with multiple corotating disks." *Journal of Fluids Engineering, Transactions of the ASME* Vol. 136 No. 8 (2014). DOI 10.1115/1.4026585.

[8] Medvitz, Richard B., Boger, David A., Izraelev, Valentin, Rosenberg, Gerson and Paterson, Eric G. "Computational fluid dynamics design and analysis of a passively suspended tesla pump left ventricular assist device." *Artificial Organs* Vol. 35 No. 5 (2011): pp. 522–533. DOI 10.1111/j.1525-1594.2010.01087.x.

[9] Schosser, Constantin. "Experimental and numerical investigations and optimisation of Tesla-radial turbines." Thesis, University of Munich. 2016.

[10] Hasinger, S. H. and Kehrt, L. G. "Investigation of a Shear-Force Pump." *Journal of Engineering for Power* Vol. 85 (1963): pp. 201–206. DOI https://doi.org/10.1115/1.3675259.

[11] Rice, Warren. "An Analytical and Experimental Investigation of Multiple-Disk Turbines." *Journal of Engineering for Gas Turbines and Power* Vol. 87 (1965): pp. 29–36. DOI https://doi.org/10.1115/1.3678134.

[12] William Beans, E. "Investigation into the performance characteristics of a friction turbine." *Journal of Spacecraft and Rockets* Vol. 3 No. 1 (1966): pp. 131–134. DOI 10.2514/3.28398.

[13] Morris, J. "Performance of Multiple Disk Rotor Pumps with Varied Interdisk Spacings." Technical report no. David W. Taylor Naval Ship Research and Development Center, Bethesda. 1973.

[14] Romanin, Vince D. "Theory and Performance of Tesla Turbines." Thesis, University of California, Berkeley. 2012. URL arXiv:1011.1669v3.

[15] Krishnan, Vedavalli G., Romanin, Vince, Carey, Van P. and Maharbiz, Michel M. "Design and scaling of microscale Tesla turbines." *Journal of Micromechanics and Microengineering* Vol. 23 No. 12 (2013). DOI 10.1088/0960-1317/23/12/125001.

[16] Holland, Kris. "Design, construction, and testing of a Tesla Turbine." Thesis, Laurentian University. 2015. URL https://zone.biblio.laurentian.ca/bitstream/10219/2533/1/FinalThesisApprovedkris_holland.pdf.

[17] Song, Jian, dong Ren, Xiao, song Li, Xue, wei Gu, Chun and ming Zhang, Ming. "One-dimensional model analysis and performance assessment of Tesla turbine." *Applied Thermal Engineering* Vol. 134 No. August 2017 (2018): pp. 546–554. DOI 10.1016/j.applthermaleng.2018.02.019. URL https://doi.org/10.1016/j.applthermaleng.2018.02.019.

[18] Katopodes, N. D. *Ideal Fluid Flow*. Butterworth Heinemann (2019). DOI 10.1016/b978-0-12-815489-2.00006-x. URL https://doi.org/10.1016/B978-0-12-815489-2.00006-X.

[19] Menter, F. R., Sechner, R. and Matyushenko, A. "Best Practice: RANS Turbulence Modeling in Ansys CFD." Technical report no. ANSYS Inc. 2021. URL https://www.ansys.com/content/dam/amp/2022/february/asset-creation/best-practices-campaign/BestPractice-RansturbulencemodelinginAnsysCFD.pdf.

[20] Omidi, Mohammad, Liu, Shu-Jie, Mohtaram, Soheil, Lu, Hui-Tian and Zhang, Hong-Chao. "Improving Centrifugal Compressor Performance by Optimizing the Design of Impellers Using Genetic Algorithm and Computational Fluid Dynamics Methods." *Sustainability* Vol. 11 (2019). DOI https://doi.org/10.3390/su11195409.

[21] Boyce, M. P. *Gas Turbine Engineering Handbook*, 2nd ed. Butterworth-Heinemann, Boston (2002).

[22] Stepanoff, A. J. *Centrifugal and Axial Flow Pumps: Theory, Design, and Application*. John Wiley & Sons, New York (1957).

[23] Knapp, Axel, Böhle, Martin and Roclawski, Harald. "Investigation of different design methods of volutes with circular cross sections for a single-stage centrifugal pump." *Open Archives of the 17th International Symposium on Transport Phenomena and Dynamics of Rotating Machinery, ISROMAC 2017*. 2017. URL https://hal.archives-ouvertes.fr/hal-02980987.

[24] ASME. "Procedure for Estimation and Reporting of Uncertainty Due to Discretization in CFD Applications." *Journal of Fluids Engineering* Vol. 130 No. 7 (2008). DOI 10.1115/1.2960953. URL http://fluidsengineering.asmedigitalcollection.asme.org/article.aspx?articleid=1434171.

[25] ANSYS. *ANSYS CFX-Pre User's Guide*. ANSYS Inc. (2013). URL http://www.ansys.com.

[26] Khait, Anatoliy, Noskov, Alexander, Alekhin, Vladimir and Bianco, Vincenzo. "Analysis of the local entropy generation in a double-circuit vortex tube." *Applied Thermal Engineering* Vol. 130 (2018): pp. 1391–1403. DOI 10.1016/j.applthermaleng.2017.11.136. URL https://linkinghub.elsevier.com/retrieve/pii/S1359431117341637.

[27] Bejan, Adrian. "Entropy generation minimization: The new thermodynamics of finite-size devices and finite-time processes." *Journal of Applied Physics* Vol. 79 No. 3 (1996): pp. 1191–1218. DOI 10.1063/1.362674. URL http://aip.scitation.org/doi/10.1063/1.362674.

[28] Izraelev, Valentin and et al. "A Passively-Suspended Tesla Pump Left Ventricular Assist Device." *ASAIO J.* Vol. 155 (2009): pp. 556–561. DOI 10.1097/MAT.0b013e3181bae73e.



https://dspace.org/

Insights into the flow field and performance of a boundary layer pump

Rajendran, David John; Palaveev, Kyril; Anselmi Palma, Eduardo; Santhanakrishnan, Mani Sekaran; Pachidis, Vassilios

2024-06-01
American Society of Mechanical Engineers (ASME)
https://doi.org/10.1115/1.4063834
Rajendran DJ, Palaleev K, Anselmi E, et al., (2023) Insights into the flow field and performance of a boundary layer pump. Journal of Engineering for Gas Turbines and Power, Volume 146, Issue 6, June 2024, Article number 061002, Paper number GTP-23-1390

Downloaded from a DSpace repository. https://dspace.org/